

DRAFT VERSION AUGUST 10, 2021

Typeset using L^AT_EX **preprint** style in AASTeX63

Idealized 2D Cloud-Resolving Simulations for Tidally Locked Habitable Planets

QIYU SONG,¹ JUN YANG,¹ HANG LUO,¹ CHENG LI,² AND SHIZUO FU^{3,4}

¹*Department of Atmospheric and Oceanic Sciences, School of Physics, Peking University, Beijing 100871, China.*

²*Department of Climate and Space Sciences and Engineering, University of Michigan, Michigan 48109, USA*

³*Key Laboratory for Humid Subtropical Eco-Geographical Processes of the Ministry of Education, Fujian Normal University, Fuzhou 350007, China*

⁴*School of Geographical Sciences, Fujian Normal University, Fuzhou 350007, China*

(Received received date; Revised revised date; Accepted accepted date)

Submitted to ApJ

ABSTRACT

Cloud is critical for planetary climate and habitability, but it is also one of the most challenging parts of studying planets in and beyond the solar system. Previous simulations using global general circulation models (GCMs) found that for 1:1 tidally locked (i.e., synchronously rotating) terrestrial planets with oceans, strong convergence and convection produce optically thick clouds over the substellar area. One obvious weakness of these studies is that clouds are parameterized based on the knowledge on Earth, and whether it is applicable to exoplanetary environment is unknown. Here we use a cloud-resolving model (CRM) with high resolution (2 km) in a two-dimensional (2D) configuration to simulate the clouds and circulation on tidally locked aqua-planets. We confirm that the substellar area is covered by deep convective clouds, the nightside is dominated by low-level stratus clouds, and these two are linked by a global-scale overturning circulation. We further find that a uniform warming of the surface causes the width of convection and clouds to decrease, but a decrease of day-night surface temperature contrast or an increase of longwave radiative cooling rate causes the width of convection and clouds to increase. These relationships can be roughly interpreted based on some simple thermodynamic theories. Comparing the results between CRM and GCM, we find that the results are broadly similar although there are many significant differences. Future work is required to use 3D CRM(s) with realistic radiative transfer and with the Coriolis force to examine the clouds and climate of tidally locked planets.

1. INTRODUCTION

Tidally locked terrestrial planets around M and K dwarfs are the most probable candidates for finding potentially habitable worlds beyond Earth. The lifetime of the host stars is longer than other main-sequence stars, and the distances between potentially habitable planets and the stars are

relatively small, thus the transits of these planets are more frequent and significant, which means more opportunity to observe them. In this study, we focus on the climate simulations of tidally locked habitable planets, in particular on convection and clouds.

Using atmospheric general circulation models (GCMs) or coupled atmosphere-ocean GCMs, previous climate simulations showed that the dayside of 1:1 tidally locked (or called synchronously rotating) habitable planets would be covered by deep convective clouds, and the nightside would be covered by low-level stratus clouds. The two hemispheres are connected with each other through a global-scale atmospheric overturning circulation, or called global-scale Walker circulation, with strong upwelling and low-level convergence over the substellar region and weak downwelling and low-level divergence in the rest of the planetary atmosphere (e.g., [Joshi et al. 1997](#); [Merlis & Schneider 2010](#); [Wordsworth, R. D. et al. 2010](#); [Edson et al. 2011](#); [Yang et al. 2013](#); [Menou 2013](#); [Kopparapu et al. 2016, 2017](#); [Wolf 2017](#); [Salameh 2017](#); [Boutle et al. 2017](#); [Haqq-Misra et al. 2018](#); [Yang et al. 2019a](#); [Del Genio et al. 2019](#)). The atmospheric circulation is largely driven by the continuous stellar heating on the permanent dayside and the longwave cooling on the permanent nightside. The dayside convective clouds strongly reflect the stellar radiation, increase the planetary albedo, and thereby cool the surface. These clouds make the inner edge of the habitable zone be closer to the host stars, expanding the width of the habitable zone.

However, GCMs have some essential shortcomings, mainly rising from their low resolution, which is on the order of hundreds of kilometers in the horizontal direction. As the low resolution is insufficient to simulate the convection and cloud processes explicitly, GCMs usually employ parameterization schemes for convection and clouds, which are based on observations and cloud-resolving simulations of Earth. Whether these parameterization schemes could be applied to exoplanets' conditions is unknown, and different models employ different parameterization schemes. Recent model intercomparisons for tidally locked planets ([Yang et al. 2019b](#); [Fauchez et al. 2020](#)) showed that there are large differences among the models in simulating the climate. Under given stellar flux, given greenhouse gas concentration and the same boundary conditions (such as a uniform slab ocean at the surface), the simulated surface temperature difference in global mean could be as large as 20 K to 30 K. The underlying reasons are mainly cloud parameterization, radiation calculation accuracy for water vapor and relative humidity (which is associated with large-scale atmospheric circulation), and the largest difference comes from clouds ([Yang et al. 2016, 2019b](#)). Improving our understanding of clouds and their effects on climate on tidally locked planets is in urgent need.

Two ways could be used to improve the studies of clouds on tidally locked habitable planets. One is to observationally identify clouds on terrestrial exoplanets, but it is far beyond the ability of present and near-future space and ground telescopes. The other one is to resolve the cloud-formation processes in exoplanets' atmospheres, which is considered in this study. Until now, there are three cloud-resolving studies for tidally locked planets around M dwarfs, [Zhang et al. \(2017\)](#), [Sergeev et al. \(2020\)](#), and [Lefèvre et al. \(2021\)](#). Due to computation resource limits, only a limited-area domain is cloud-resolved, ≈ 1000 by 1000 km in [Zhang et al. \(2017\)](#), 6000 by 6000 km in [Sergeev et al. \(2020\)](#), and 250 by 250 km in [Lefèvre et al. \(2021\)](#). [Zhang et al. \(2017\)](#) found that there are strong spatial variability in clouds, shortwave radiation, and surface temperature even in the small domain. This is likely due to the small scales of deep convection. [Sergeev et al. \(2020\)](#) examined the dependence of the simulated climate on the choice of convection parameterization scheme and a cloud-permitting modeling of the substellar convection. They found that the simulated

clouds, precipitation, atmospheric circulation, and day-to-night energy transport are sensitive to how convection and clouds are treated. They also showed that the planetary albedo of the substellar region in the cloud-permitting simulation is somewhat higher than that in the simulation with parameterized convection and clouds. [Lefèvre et al. \(2021\)](#) confirmed that the substellar region of tidally locked habitable planets should be covered by convective clouds. They also found that there are large differences in the simulated cloud albedo between the CRM and GCMs, due to less formation of low-altitude stratocumulus clouds in the CRM they employed. There are two weaknesses in these cloud-resolving simulations. One is that the cloud-resolving domain is too small to represent the entire clouds over the wide convective area on the dayside. The other one is that the effects of large-scale circulation (such as water vapor converging towards the substellar area) on the convection is not well represented, or the interaction between the cloud-resolving area and the large-scale circulation is absent in their experimental designs.

In the cloud-resolving experiments for Earth, the horizontal resolution is always several kilometers or even less, and the time step is always in the order of seconds (e.g., [Miller & Pearce 1974](#); [Klemp & Wilhelmson 1978](#); [Tao & Soong 1986](#); [Tomita et al. 2005](#); [Muller & Held 2012](#); [Wofsy & Kuang 2012](#)), both of which are at least two orders smaller than those in GCMs, so lots of computation resources as well as storage disks are required. Due to the very high computation resource requirement, cloud-resolving simulations always employ a 2D configuration or a regional 3D configuration (e.g., [Muller & Held 2012](#); [Wofsy & Kuang 2012](#)). Even for Earth, only few studies have employed global or near-global cloud-resolving simulations (e.g., [Tomita et al. 2005](#); [Bretherton & Khairoutdinov 2015](#); [Khairoutdinov & Emanuel 2018](#); [Narenpitak & Bretherton 2019](#); [Stevens et al. 2019](#)). As a further step using the method of cloud-resolving, we simulate the clouds on tidally locked habitable planets in a 2D configuration (longitude–height) but in a large zonal (west–east) domain, 40,000 km, encircling the entire equator of the planet. The domain is large enough to consistently investigate the interaction between convection/clouds and large-scale circulation, but the meridional (south–north) direction is absence in this study.

Previous studies showed that for the Walker Circulation over the Pacific Ocean on Earth, a 2D model configuration along the equator is very useful in studying the effects of sea surface temperature, surface temperature gradient, radiative transfer, cloud microphysics, and other factors on the sensitivities of the Walker Circulation and clouds ([Grabowski et al. 2000](#); [Bretherton & Sobel 2002](#); [Bretherton et al. 2006](#); [Wofsy & Kuang 2012](#); [Liu & Moncrieff 2008](#); [Byrne & Schneider 2016](#); [Chen & Wu 2019](#)). As the atmospheric circulation on tidally locked terrestrial planets has certain similarities with the Walker circulation on Earth (e.g., [Joshi et al. 1997](#); [Edson et al. 2011](#); [Merlis & Schneider 2010](#); [Yang et al. 2013](#)), we employ a similar 2D model configuration. On Earth, the main upwelling occurs over the warm pool of the western Pacific, and the main downwelling occurs over the cold tongue of the eastern Pacific. On tidally locked planets, the upwelling is mainly over the substellar area and the downwelling over the rest of the planet. But there are two main differences between our configuration and the configurations widely used for the Walker Circulation simulations on Earth: one is that the spatial scale is larger, 40,000 km for a whole circle along the equator versus $\approx 20,000$ km for the width of the Pacific ocean, and the other one is that the zonal (west–east) temperature difference is tens of degrees versus several degrees in K or $^{\circ}\text{C}$. Therefore, the results shown here are more applicable for tidally locked planets than for the regional Walker Circulation on Earth.

The structure of this paper is as follows. In Section 2, we introduce the CRM used in this study and address the experimental designs. Corresponding GCM experimental designs are also shown. In Section 3, we first show the general characters of the cloud pattern and the large-scale circulation. Then, we study the effects of different factors on the clouds and circulation, including making uniform surface warming or cooling, varying the day-night surface temperature contrast, and changing the strength of atmospheric radiative cooling, and then explore the underlying mechanisms (subsections 3.2 and 3.3). The comparisons between CRM and GCM are shown in subsection 3.4. Finally, we draw the summary in Section 4.

2. MODEL DESCRIPTIONS AND EXPERIMENTAL DESIGNS

2.1. 2D CRM Simulations

The model used here is the Simulating Nonhydrostatic Atmospheres of Planets (SNAP, Li & Chen (2019), link: <https://snap.chengcli.io/>), a nonhydrostatic CRM, developed for performing high-resolution studies including moist convection and cloud processes in planetary atmospheres of various types of planets. The model employs the finite volume method to solve the hydrodynamic equations including density, velocities, vapor, cloud, precipitation, and total energy, because this method maintains conservation quantities and deals well with variables with large gradients. The equations of the model are originally written in a 3D space, but one horizontal dimension (y direction) is left out in this work because we perform simulations in a 2D space.

The continuity equations of different components in the atmosphere are written as:

$$\frac{\partial \rho_i}{\partial t} + \frac{\partial (\rho_i u)}{\partial x} + \frac{\partial (\rho_i w)}{\partial z} = 0, \quad i = d, v, c \quad (1)$$

$$\frac{\partial \rho_p}{\partial t} + \frac{\partial (\rho_p u)}{\partial x} + \frac{\partial (\rho_p w)}{\partial z} = -\frac{\partial (\rho_p \bar{w}_p)}{\partial z}, \quad (2)$$

where ρ_d, ρ_v, ρ_c , and ρ_p represent the density of dry air, water vapor, cloud, and precipitation, respectively. (u, w) are the 2D velocity components in (x, z) directions. \bar{w}_p is the terminal velocity of precipitation with respect to the mean velocity of the background atmosphere and is set to -10 m s^{-1} in all cases, where minus value means moving downwards.

The difference in vertical velocity between precipitation and the background atmosphere also contributes to vertical momentum and energy fluxes. The momentum equations are written as:

$$\frac{\partial (\rho u)}{\partial t} + \frac{\partial (u \rho u)}{\partial x} + \frac{\partial (w \rho u)}{\partial z} = -\frac{\partial p}{\partial x} - \frac{\partial (\bar{w}_p \rho_p u)}{\partial z} \quad (3)$$

$$\frac{\partial (\rho w)}{\partial t} + \frac{\partial (u \rho w)}{\partial x} + \frac{\partial (w \rho w)}{\partial z} = -\frac{\partial p}{\partial z} - \rho g - \frac{\partial (\bar{w}_p \rho_p w)}{\partial z}, \quad (4)$$

where $\rho = \rho_d + \rho_v + \rho_c + \rho_p$ is the total density, and $p = \rho_d R_d T + \rho_v R_v T$ is the total pressure of water vapor and dry air, which are both treated as idealized gases.

The total energy of an air parcel with heterogeneous components consists of internal energy, kinetic energy, and chemical potential energy. The chemical potential energy marks the change in latent heat in phase transitions and is set to zero for gases as a benchmark. The total energy per volume (ρe) is written as:

$$\rho e = \rho_d c_{v,d} T + \rho_v c_{v,v} T + (\rho_c + \rho_p) c_l T + \frac{1}{2} \rho (u^2 + w^2) + \mu_v \rho_v + \mu_l (\rho_c + \rho_p), \quad (5)$$

where $c_{v,d}$, $c_{v,v}$, and c_l represent the heat capacity at constant volume of dry air, water vapor, and liquid water (including cloud and precipitation water), respectively. μ_v represents the chemical potential of vapor water, and μ_l represents that of liquid water, and both of them change with air temperature (T). Gravity potential energy is not included in the above equation; instead, the gravity force is treated as an external force to the parcel in Equation (4).

From the continuity equations and momentum equations we can derive the energy equation:

$$\frac{\partial(\rho e)}{\partial t} + \frac{\partial(u\rho e)}{\partial x} + \frac{\partial(w\rho e)}{\partial z} = -\rho g w - \rho_p g \bar{w}_p - \frac{\partial(u p)}{\partial x} - \frac{\partial(w p)}{\partial z} - \frac{\partial(\bar{w}_p \rho_p e_p)}{\partial z} + \rho \bar{c} \dot{Q}, \quad (6)$$

where $e_p = c_l T + \frac{1}{2}(u^2 + w^2) + \mu_l$ is the specific total energy of precipitation, and $\bar{c} = (\rho_d c_{v,d} T + \rho_v c_{v,v} T + (\rho_c + \rho_p) c_l T) / \rho$ is the average heat capacity of every component. \dot{Q} is the diabatic energy source and sink with the units of K s^{-1} , including latent heating and radiative cooling. Note that shortwave radiation is not included in the simulations.

The microphysical processes in the hydrological cycle are described by the Kessler scheme (Kessler 1969) written as:

$$\frac{\partial q_v}{\partial t} = -k_1 (q_v - q_v^*)^+ + k_4 q_p (q_v^* - q_v)^+ \quad (7)$$

$$\frac{\partial q_c}{\partial t} = k_1 (q_v - q_v^*)^+ - k_3 q_c q_p - k_2 q_c \quad (8)$$

$$\frac{\partial q_p}{\partial t} = -k_4 q_p (q_v^* - q_v)^+ + k_3 q_c q_p + k_2 q_c. \quad (9)$$

where q_v , q_c , and q_p represent mass mixing ratios of water vapor, cloud water, and precipitation water, respectively. Note that the ice phase of clouds is not included in this model. The k_1 term is the condensation of over-saturated water vapor and is a rapid process that can be treated as an instant process. The rate of the condensation is proportional to the over-saturated mixing ratio $(q_v - q_v^*)^+$, where q_v^* is the saturation water vapor mixing ratio, and the expression of $(\cdot)^+$ means taking the maximum of the in-bracket term and zero, i.e., $\max(\cdot, 0)$. The k_2 term is the auto-conversion from cloud water to precipitation water. The k_3 term is the accretion of cloud and rain droplets, which is taken as zero in our simulations. The k_4 term is the re-evaporation term of precipitation back to vapor when a raindrop enters a sub-saturate air parcel. We performed two series of sensitivity tests of the microphysical parameters k_2 and k_4 in the Appendix at the end of this paper.

The atmosphere in our simulations is configured based on Earth's atmosphere, with gravity (g) of 9.81 m s^{-2} and dry atmosphere gas constant (R_d) of $287 \text{ J K}^{-1} \text{ kg}^{-1}$. The domain simulated is 2D along the equator, which means there is no Coriolis force. The size of the domain is 35 km in height and 40,000 km in the zonal direction, representing the global atmosphere over the Equator of an Earth-size planet. The horizontal resolution is 2 km, and the vertical resolution is 250 m (uniform, a simple set). The CFL number is set to 0.6, which means a time step of about 2 s. Sub-grid entrainment and detrainment are not included. There is no realistic radiation transfer process for either gases or clouds in the model. The longwave radiation is simulated simply by imposing a fixed radiative cooling rate everywhere (by default). As the heating effect of ozone gas by absorbing ultraviolet radiation is not calculated in the model, we set a minimum stratospheric temperature (T_{st}) of 170 K to represent the stratosphere: when the air temperature drops below the value of T_{st} , a Newtonian adjustment back to T_{st} is employed.

We use periodic boundary condition in zonal direction and reflecting boundary condition in vertical direction. A sponge layer is added within the top 5 km of the model (H_{top}) to absorb unrealistic reflecting gravity waves from the model top. A simple friction layer of 1 km (H_{low}) is added at the bottom of the model as a momentum dissipation to simulate the effect of boundary layer turbulence and surface friction. Both the sponge and dissipation layers share the idealized form of:

$$\frac{du(z)}{dt} = -\frac{u}{\tau_i} \sin^{1/2} \left(\frac{\pi}{2} \frac{H_i - \Delta z}{H_i} \right), \quad i = top, low, \quad (10)$$

with τ_{top} is 2 hrs, and τ_{low} is also 2 hrs by default. Δz is the distance between the altitude (z) and the top or lower boundary. We performed one series of sensitivity tests of the lower boundary friction parameter τ_{low} in the Appendix.

Table 1. Experimental Designs Using the Cloud-Resolving Model SNAP

	Description	Value
L	domain length (km)	40,000
H	domain height (km)	35
Δx	horizontal resolution (km)	2
Δz	vertical resolution (m)	250
T_s^{max}	maximum surface temperature in the control run (K)	310
ΔT_s	day-night surface temperature contrast in the control run (K)	50
R_c	radiative cooling rate in the control run (K day^{-1})	-1.89
τ_{low}	surface friction time scale (hrs)	2
k_2	conversion rate (cloud to precipitation) (s^{-1})	10^{-4}
k_4	re-evaporation rate (rain droplets to vapor) (s^{-1})	10^{-2}
Group 1	uniformly changing surface temperature T_s (K)	230_280 ^a , 240_290, 250_300, 260_310
Group 2	changing surface temperature contrast ΔT_s (K)	260_310, 275_310, 290_310, 305_310
Group 3	changing radiative cooling rate R_c (K day^{-1})	-0.945, -1.89, -3.78

NOTE—a. The values are the minimum and maximum values of surface temperature, respectively (Figure 1).

In our simulations, surface temperatures (T_s) are fixed (see Figure 1), and their values are set roughly according to the simulated equatorial results of GCMs coupled to a slab ocean: on the dayside where $|x| < L/4$, $T_s(x) = T_s^{min} + \Delta T_s \cos^{1/2}(2\pi x/L)$, and on the nightside where $|x| \leq L/4$, $T_s(x) = T_s^{min}$. Here L is the domain width, and x varies from $-L/2$ to $L/2$. The power of $1/2$ is used due to the weak temperature gradient in the substellar area and the strong temperature gradient near the western and eastern terminators. A plot of T_s in different experiments is shown in Figure 1. In the control experiment, T_s^{min} is 260 K, and ΔT_s is 50 K.

In calculating the surface fluxes of sensible heat and latent heat, the common treatments are discussed in Pierrehumbert (2010). But since the model employed in this study is originally developed for simulating the atmosphere of gas giants, it does not have a detailed surface scheme yet. In the model, the surface fluxes of sensible heat and latent heat are simplified calculated using a Newtonian

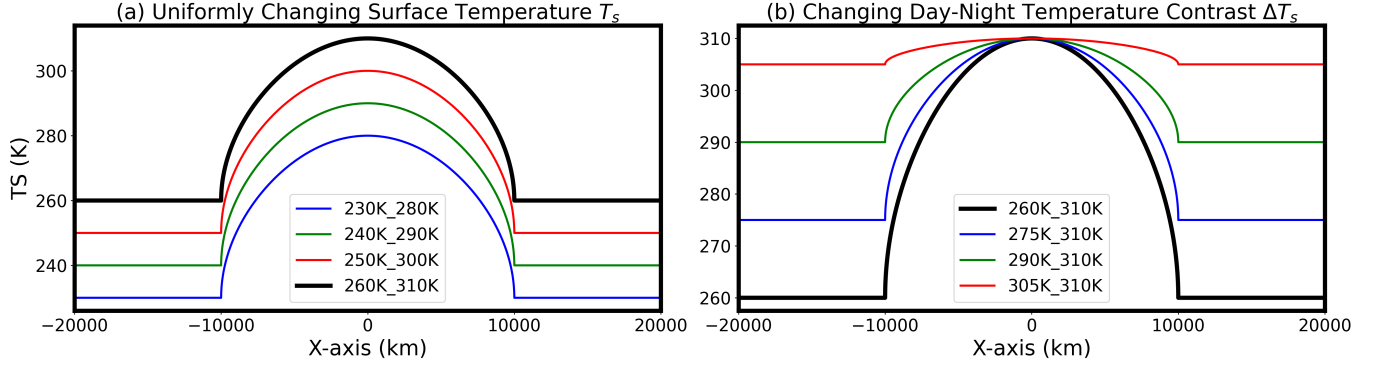


Figure 1. The surface temperature (T_s) distribution in the CRM experiments: (a) the group of uniformly changing T_s by intervals of 10 K; (b) changing day-night T_s contrast by intervals of 15 K while fixing the maximum T_s (310 K). The black line is the control experiment. The substellar point is at $x = 0$, and the terminator line is at $x = \pm 10,000$ km. The legends show the minimum and maximum values of T_s .

adjustment. The surface is adjusted to the specified surface temperatures and the saturated water mixing ratio at the corresponding surface temperatures within the time scale of τ_{sf} . The value of τ_{sf} is two hours. These treatments capture the essential features that sensible and latent fluxes are proportional to the temperature and moisture differences between near-surface air and the surface.

We performed three groups of experiments to examine the responses of convection and clouds to different environmental settings, including varying the surface temperature everywhere uniformly, reducing the day-night surface temperature contrast, and changing the radiative cooling rate. Table 1 summarises the experimental designs of the control experiment and the three different groups of experiments. Each experiment is run for different lengths of time to reach equilibrium, ranging from 30 to 100 Earth days. Then, an additional 20 Earth days of simulation is run to obtain the data for calculating the mean equilibrium states shown below.

2.2. 3D GCM Simulations

In order to compare the results of CRM with those of GCM, we did three groups of GCM experiments: the first group is for uniformly changing the surface temperature everywhere, the second group is for reducing the day-night temperature contrast, and the third group is for varying the stellar flux when the surface is coupled to a slab ocean. In the first and second groups, the stellar flux is fixed (1200 W m^{-2}), and the surface temperatures are specified, as shown in subsection 3.4 below. In the third group, the model is coupled with a 50 m mixed layer, immobile ocean, and ocean heat transport is specified to be zero everywhere. A series of stellar fluxes are used in the third group, 1200, 1400, 1600, 1800, 2000, and 2200 W m^{-2} . When the stellar flux increases, the surface temperature increases everywhere, and meanwhile the day-night surface temperature contrast decreases since the night-side surface warms more than the day-side surface.

The GCM we employed is the 3D Community Atmospheric Model version 3, called CAM3 (Collins et al. 2004), which is developed by the National Center for Atmospheric Research to simulate the climate of Earth. The model solves the primitive equations for atmospheric motion with a spectral Eulerian core on a rotating sphere. The radiative transfer model in CAM3 is based on Ramanathan & Downey (1986) and Briegleb (1992) with the updates described in Collins et al. (2004). The

radiation calculation includes the effects of water vapor, greenhouse gases, and clouds. The model uses subgrid-scale parameterizations to model deep and shallow/middle convection, condensation, precipitation, and evaporation of precipitating droplets (Sundqvist 1988; Zhang & McFarlane 1995; Rasch & Kristjánsson 1998; Zhang et al. 2003). Clouds are parameterized into three categories: marine stratus clouds, layered clouds, and convective clouds. Cloud fraction and the associated optical properties are evaluated via a diagnostic method. The diagnosis is a generalization of the scheme introduced by Slingo (1987), with variations described in Hack et al. (1993), Kiehl et al. (1998), and Rasch & Kristjánsson (1998). The model has 26 vertical levels from the surface to the middle stratosphere (≈ 3 hPa) at the horizontal resolution of T42, which is 2.8° in latitude by 2.8° in longitude.

All the experiments are set to be 1:1 tidally locked, which means the rotation period is equal to the orbital period. The orbital period is set to be 30 Earth days. The stellar temperature is set to be 3400 K. The atmosphere is Earth-like, including N_2 and H_2O . CO_2 concentration is 300 parts per million by volume (ppmv), CH_4 concentration is 0.8 ppmv, and N_2O is 0.27 ppmv. There is neither aerosol nor ozone. The model is coupled to a thermodynamic sea ice model, in which sea ice flows are not considered. In the first and second groups, each case is integrated for 30 Earth years and reaches a steady state after about 20 years. In the third group, each case is integrated for about 60 Earth years and reaches a steady state after about 40 years. Averages over the last 5 years are used for our analyses below.

3. RESULTS

3.1. *Results of the 2D CRM simulations*

In the control experiment, exerted by the centrally-peaked surface temperature pattern and spatially-uniform radiative cooling pattern, the most dominant character of the simulation results is the deep convection clouds in the substellar area (Figure 2; for more clearly view the clouds, please watch the online video 1). The deep convection clouds are coupled with a global-scale Walker-like circulation that covers the whole troposphere (Figure 3(l)). The airflow convergences in the lower atmosphere, ascends in the substellar area, reaches its top at the substellar tropopause (about 25 km), flows out at the altitude between 10 and 25 km, and then descends in the region outside of the substellar area. The area of the ascending branch is much narrower than that of the descending branch. The maximum speed of the convergent winds in the lower atmosphere is about 10 m s^{-1} , and that of the divergent winds in the upper troposphere is about 30 m s^{-1} . The surface convergence/divergence is approximately symmetric about the substellar point (i.e., the location of the maximum surface temperature). In the descending branch, the low-level atmosphere is very stable as the near-surface temperature is lower than that of the bottom of the free atmosphere.

The clouds can develop to the upper troposphere in the ascending branch of the circulation (blue arrow in Figure 2(a)). In the upper troposphere (10 to 25 km) where there is strong divergence, the clouds expand towards the nightside following the strong outflow and form the wider high-level anvil clouds (red arrow in Figure 2(a)) than the mid-altitude clouds. The pattern of moisture distribution also follows the circulation (Figure 3(p)). The descending branch of the circulation forces an inversion layer below 5 km in the non-convective area (Figure 3(d)), which traps moisture below it and prohibit the night-side clouds from growing upwards (Figure 3(h)). The characteristics of

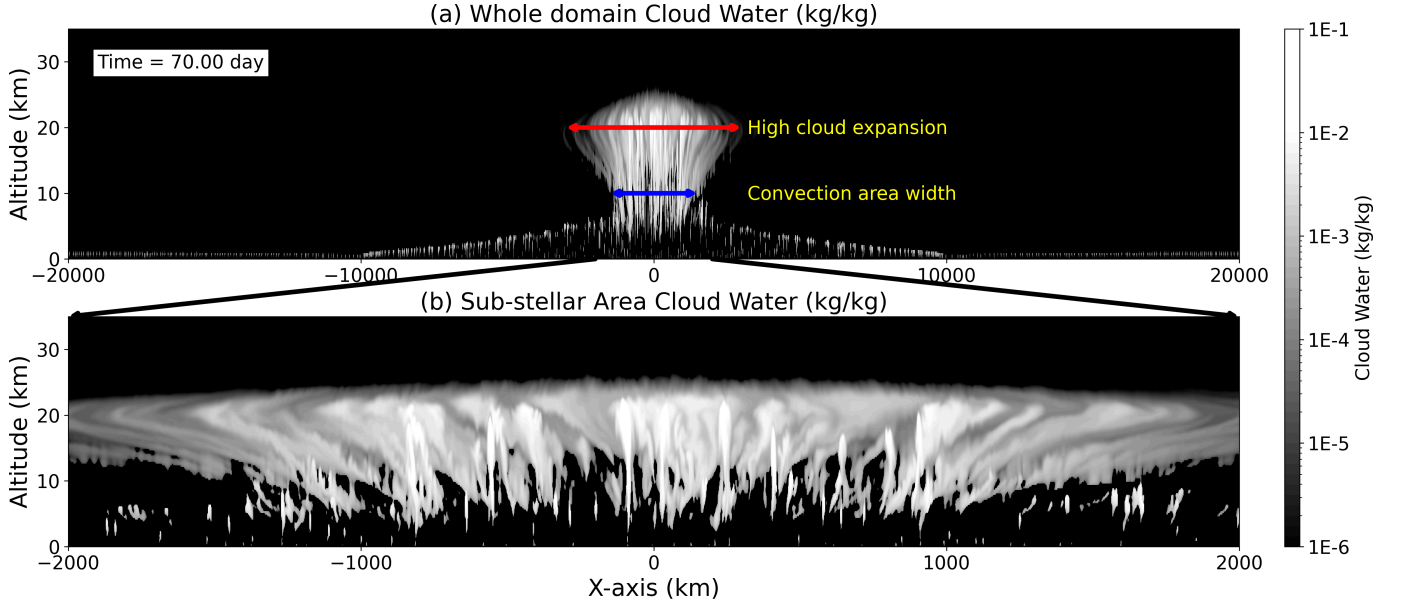


Figure 2. A snapshot of cloud water condensation in the control experiment: (a) the whole domain; (b) the substellar area. The substellar point is at $x = 0$, and the terminator lines are at $x = \pm 10,000$ km. In (a), the width of the ascending branch of the large-scale overturning circulation (or roughly the width of the deep convective cloud area) and the width of high-level anvil clouds are marked with blue arrow and red arrow, respectively. In the control experiment, the surface temperature follows the black line shown in Figure 1, and the radiative cooling rate is -1.89 K day^{-1} (a constant everywhere). To more clearly view the clouds, please watch the online video 1.

these results are similar to previous studies of equatorial-Pacific Walker circulation (Bretherton & Sobel 2002; Liu & Moncrieff 2008; Su et al. 2008; Wofsy & Kuang 2012), but our experiments hold a temperature contrast of tens of degrees between the warm region and the cool region, which is an order of magnitude larger than previous studies. These results are also similar to previous studies on tidally locked planets using GCMs (Yang et al. 2013; Kopparapu et al. 2016, 2017; Wolf 2017).

In the cloud-resolving simulations, from transient cloud snapshots, it is clear to see the high spatial variability of convection clouds in the troposphere (Figure 2). Each convection plume occupies only several model grids horizontally (about 10 km), but neighboring plumes are separated by clear-sky air with a distance of several hundred kilometers. In the upper troposphere with strong divergence, the anvil clouds of convection plumes join together to form the more smoothly distributed integral high clouds at about 20 km.

Below, we show the responses of clouds and large-scale circulation to varying the surface temperature and atmospheric radiative cooling rate. The possible reasons for the trends of the responses will be addressed in the following subsections 3.2 and 3.3.

In the first group of experiments with uniform surface warming, the height of the cloud top rises, the ascending area of the large-scale circulation shrinks, the width of the high-level anvil clouds also becomes narrower, but the strength of the ascending branch becomes stronger (Figure 3). These can be viewed from the vertically-integrated cloud water path (Figure 4(a)), surface rainfall rate (Figure 4(b)), cloud water concentration (Figure 3(f-h)), vertical velocity and horizontal velocity (Figure 3(j-l)), and relative humidity (Figure 3(n-p)). Quantitatively, in the three experiments of 240K_290K, 250K_300K, and 260K_310K (representing the minimum and maximum surface temperature in each

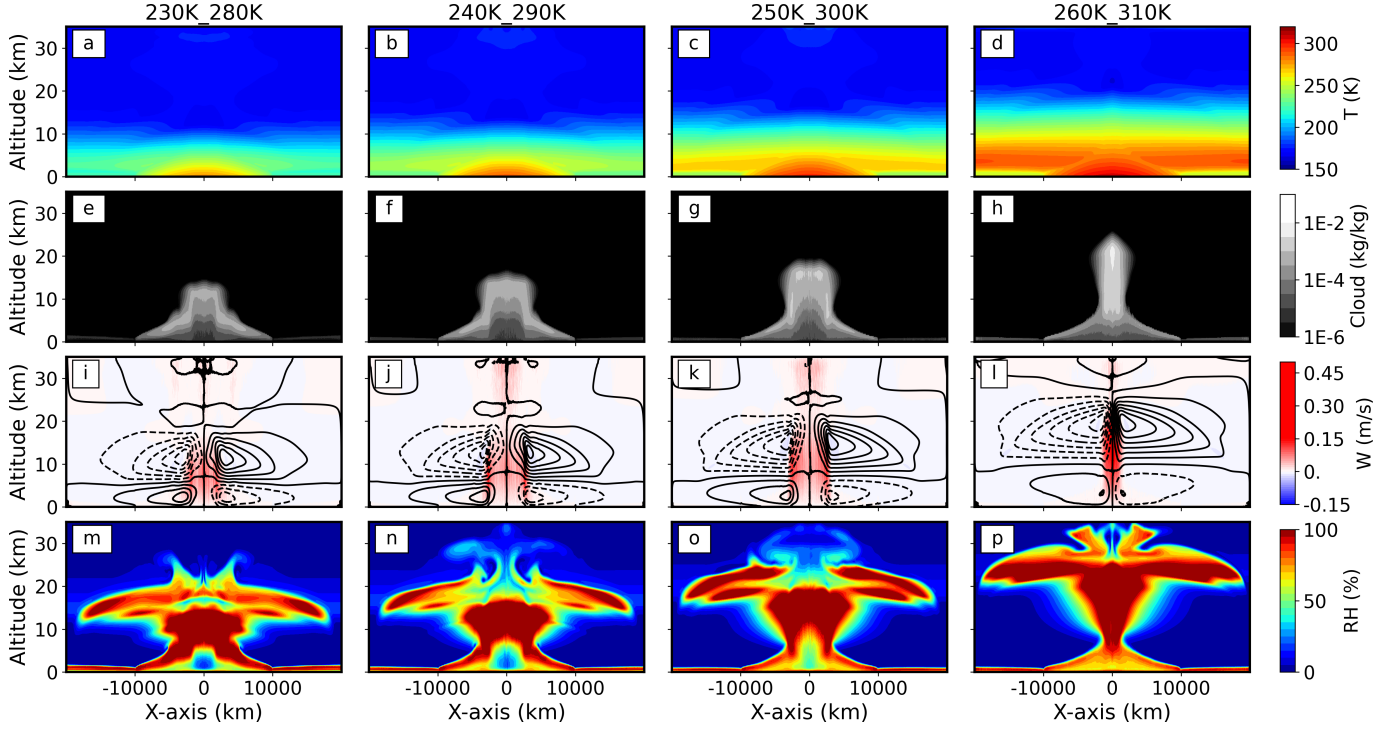


Figure 3. Responses of the atmosphere to uniform surface temperature changes. (a-d) air temperature (K), (e-h) cloud water concentration (kg kg^{-1}) in logarithmic color scale, (i-l) vertical velocity (m s^{-1} , color shaded) and horizontal velocity (contours with intervals of 5 m s^{-1} and negative lines dashed), and (m-p) relative humidity (%). The word in the top of each column, such as 230K_280K, represents the minimum and maximum surface temperatures, respectively (see Figure 1(a)).

experiment, respectively), the fractional widths of the ascending area (divided by the whole domain width) are 17.1%, 15.8%, and 7.1%, and the fractional widths of high-level anvil clouds at their respective peak altitudes are 23.0%, 22.9%, and 17.0%, respectively. The experiment of the coolest case of 230K_280K is an exception in this group, with smaller widths of the ascending area (15.5%) and of the high-level anvil clouds (18.6%) (Figure 3(e)). This exception may be due to that the surface is too cold and the convection is too weak, so that near-surface friction has a strong effect in weakening both the near-surface convergence and the substellar convection.

In the second group of experiments with decreasing day-night temperature contrast, the area of the ascending branch widens, and the width of the high-level anvil clouds also becomes wider, but the strength of the ascending/descending branches becomes weaker. These can be viewed from the vertically-integrated cloud water path (Figure 4(c)), surface rainfall rate (Figure 4(d)), cloud water concentration (Figure 5(e-h)), vertical velocity and horizontal velocity (Figure 5(i-l)), and relative humidity (Figure 5(m-p)). In the four experiments of 260K_310K, 275K_310K, 290K_310K, and 305K_310K, the fractional widths of the ascending area are 8.7%, 9.3%, 10.6%, and 15.1%, and the fractional widths of high-level anvil clouds at their respective peak altitudes are 17.0%, 17.4%, 18.2%, and 21.9%, respectively.

In the third group of experiments, when enhancing the strength of the longwave radiative cooling, both the ascending area and the high-level anvil clouds become wider, and the strength of the global overturning circulation becomes stronger. These can be viewed from the vertically-integrated cloud

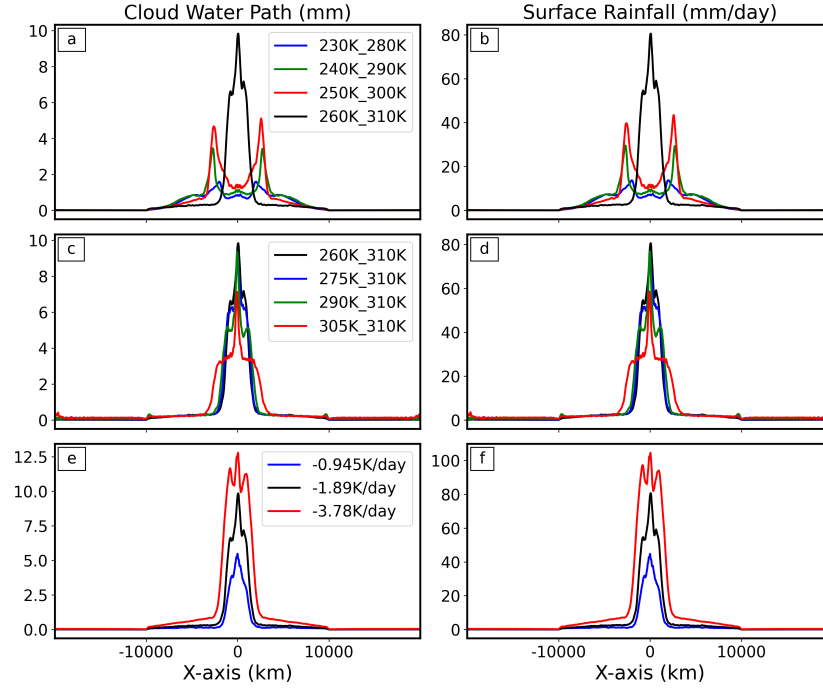


Figure 4. Effects of different environmental settings on the vertically integrated cloud water path (left column) and the surface rainfall rate (right column). Panels (a-b), (c-d), and (e-f) are for the three groups of experiments, respectively (see Table 1).

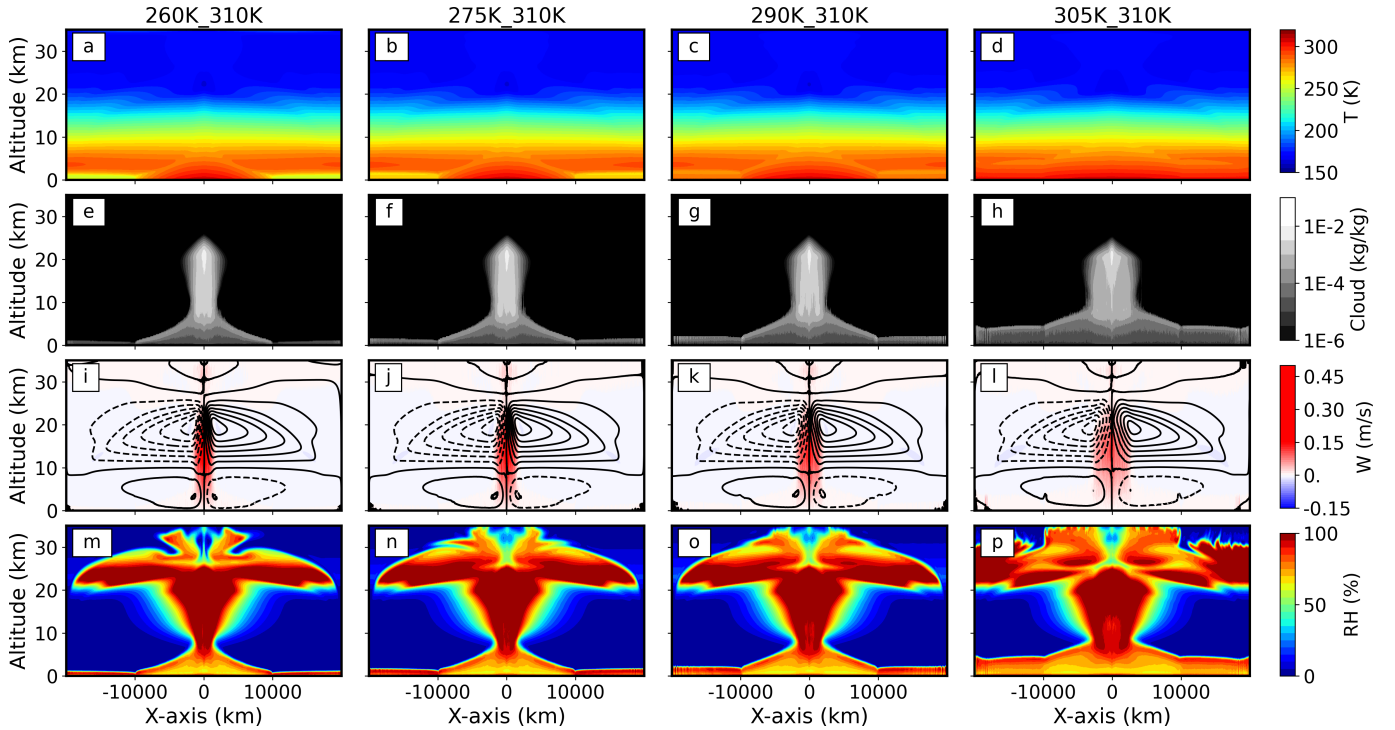


Figure 5. Same as Figure 3 but for the second group of experiments: changing day-night surface temperature contrast (see Figure 1(b)). The maximum surface temperature is 310 K in all four experiments, but the night-side surface temperature is 260, 275, 290, and 305 K, respectively.

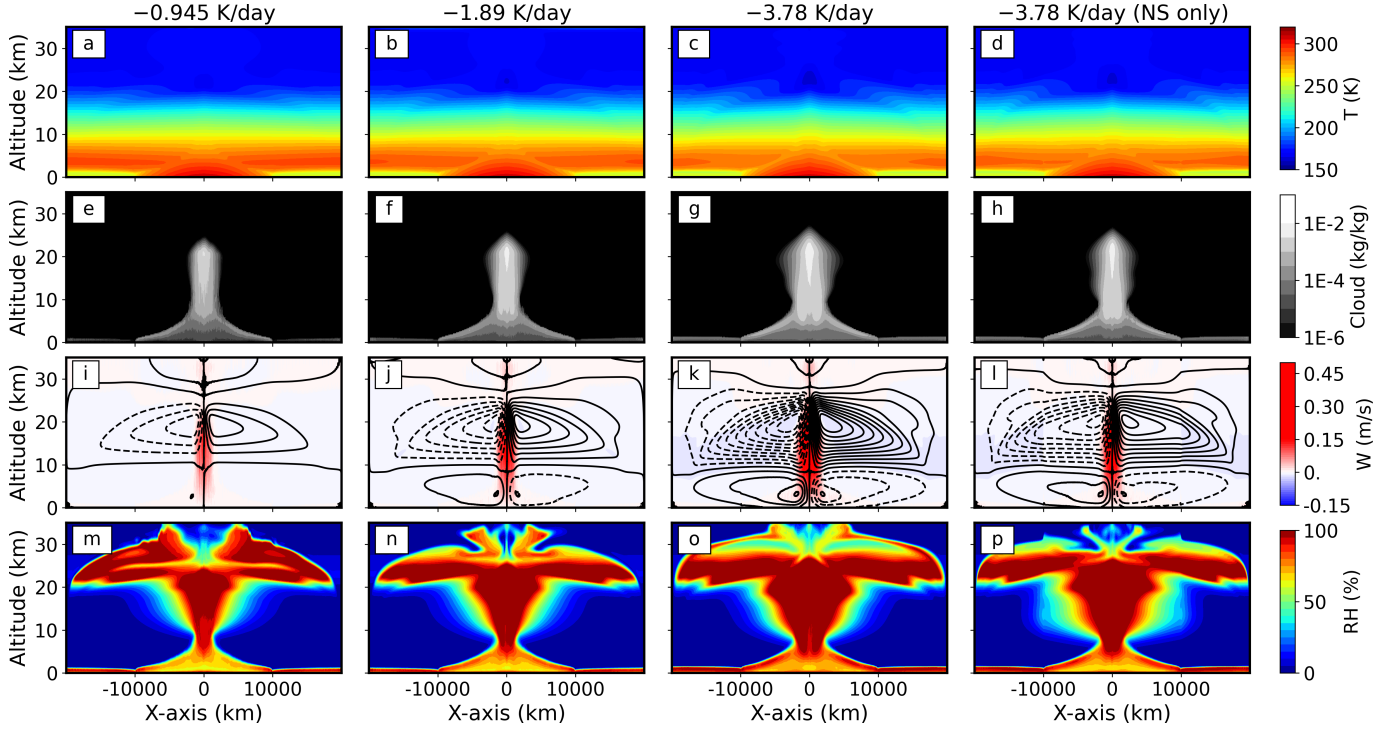


Figure 6. Same as Figure 3 but for the third group of experiments: changing the radiative cooling rate. From left to right, the radiative cooling rate is -0.945 , -1.89 (control value), and -3.78 K day^{-1} , respectively. In the fourth column, only the night-side (NS) radiative cooling rate is doubled (from -1.89 to -3.78 K day^{-1}) with the day-side radiative cooling rate, -1.89 K day^{-1} , is unchanged.

water path (Figure 4(e)), surface rainfall rate (Figure 4(f)), cloud water concentration (Figure 6(e-g)), vertical velocity and horizontal velocity (Figure 6(i-k)), and relative humidity (Figure 6(m-o)). As the radiative cooling rate strengthens from -1.89 K day^{-1} to -3.78 K day^{-1} , the atmospheric temperature drops slightly in the upper troposphere (Figure 6(a-c)). In the three experiments of -0.945 K day^{-1} , -1.89 K day^{-1} , and -3.78 K day^{-1} , the fractional widths of the ascending area are 8.6%, 8.7%, and 10.7%, and the fractional widths of high-level anvil clouds at their respective peak altitudes are 13.1%, 17.0%, and 24.6%, respectively (Figure 6(e-g)). In the added experiment of increasing the radiative cooling on the nightside only (from -1.89 K day^{-1} to -3.78 K day^{-1} ; the day-side radiative cooling is not changed; see the rightest column in Figure 6), the strength of the overturning circulation becomes stronger, and the cloud width become wider but with much smaller magnitudes, comparing to the experiment of increasing the radiative cooling of both nightside and dayside. This result suggests that both dayside and nightside radiative cooling can influence the convection and clouds.

3.2. What Determines the Width and Strength of the Convection and Large-scale Circulation?

In subsection 3.1, we have found that the widths of the ascending area and of the mid-altitude clouds decrease with uniform surface warming but increase under reduced day-night surface temperature contrast or under enhanced longwave radiative cooling. And, the strengths of the convection and large-scale circulation become stronger under uniform surface warming or enhanced longwave radiative cooling but become weaker when the day-night surface temperature contrast decreases. An

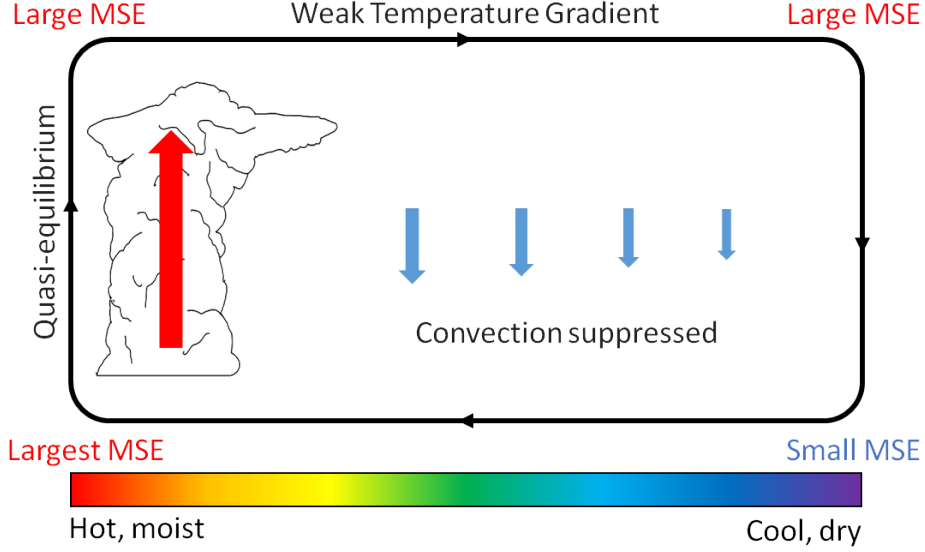


Figure 7. Conceptual illustration of the convection and large-scale atmospheric circulation. The warm and moist air in the substellar lower atmosphere results in the highest moist static energy (MSE) there, which is much larger than that of the night-side near-surface atmosphere, forming a large zonal MSE contrast. Following convective quasi-equilibrium, MSE in the upper troposphere of the substellar area is also high, close to that at the cloud base. In the free troposphere, the weak temperature gradient (WTG) approximation causes the air temperature in the free troposphere to be nearly uniform at each altitude. Therefore, on the nightside, MSE in the free atmosphere is much larger than MSE near the surface, suppressing convection activity there.

analysis of moist static energy (MSE) can roughly explain these trends. MSE is a thermodynamic variable that describes the state of a moist air parcel, and it is the sum of the parcel’s enthalpy ($c_p T$), the geopotential energy (Φ), and the latent energy ($L_v q$). The MSE is written as:

$$MSE = c_p T + \Phi + L_v q, \quad (11)$$

where q is the water vapor mixing ratio. The conceptual diagram for the process of how MSE constrains the convection and large-scale circulation on tidally locked habitable planets is shown in Figure 7. The zonal distribution of surface MSE in the three groups of experiments is shown in Figure 8. The vertical profiles of MSE and its temperature and vapor terms in the three groups are shown in Figure 9, in which the substellar profiles represent the ascending area, and the night-side profiles represent the descending area.

MSE is a useful variable because it is approximately conserved during adiabatic ascent or descent with phase changes of water between liquid and vapor (Wallace & Hobbs 2006). So, the vertical profile of MSE can be used to inform the strength of convection. In the troposphere, a constant MSE profile represents a thermodynamically neutral atmospheric stratification. When the MSE in the free atmosphere is lower than that near the surface, convection tends to develop and release the instability of the atmosphere. When the vertical structure of MSE is inverted with MSE near the surface being lower than that of the free atmosphere, the atmosphere tends to be stable.

Because the surface atmosphere in the substellar area is much warmer than that on the nightside, the day-side near-surface MSE is much greater than that of the nightside (Figure 8). In the warm

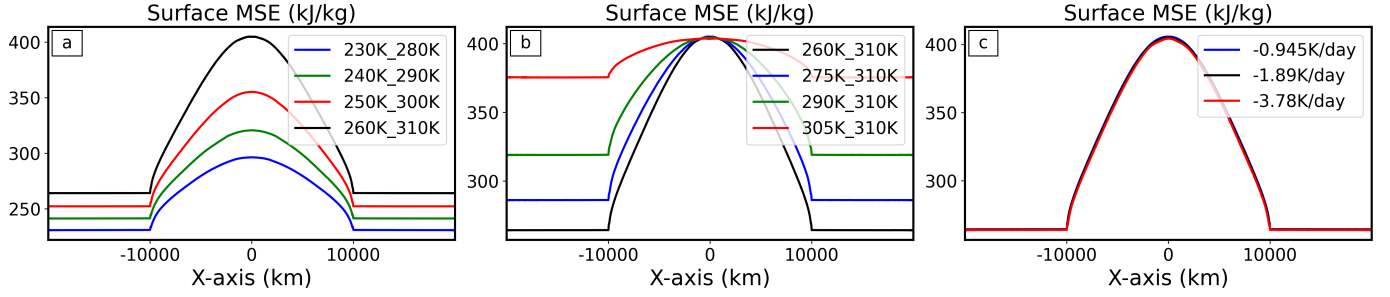


Figure 8. Surface MSE in the three groups of experiments: (a) uniformly changing the surface temperature, (b) changing the day-night surface temperature contrast, and (c) changing the radiative cooling rate.

substellar area, the atmosphere is in a quasi-equilibrium state, for which any existing buoyancy in the atmosphere can be adjusted by moist convection, and the saturated MSE in the free troposphere equals the subcloud MSE where the air parcel rises from. This adjustment process takes a very short time compared with external forcing or large-scale mean circulation because convection in the atmosphere is a fast process. As a result, the atmosphere almost stays in a quasi-equilibrium state over the substellar region, and MSE in the upper troposphere is tightly connected to MSE near the surface (Arakawa & Schubert 1974; Marquet 1993; Emanuel et al. 1994; Emanuel 2007; Neelin et al. 2008). Therefore, MSE in the free troposphere over the substellar region is also high, as shown in Figure 9(a, d, and g).

The horizontal temperature gradient in the upper troposphere is weak, satisfying the weak temperature gradient (WTG) approximation (Charney 1963; Sobel et al. 2001). This is because of the nonexistence of the horizontal Coriolis force along the equator, and thus the momentum and heat transports by gravity waves and large-scale advection in the free atmosphere are effective. Consequently, the high MSE in the substellar area can spread towards the nightside, resulting in almost uniformly high MSE in the upper troposphere of the whole domain. Therefore, on the nightside, there exists a large vertical inversion in MSE, with the value in the upper troposphere being much higher than that near the surface. The inversion area also extends across the terminator lines, occupying a large area of the dayside. This MSE inversion implies that the atmosphere is stable, and convection activity is prohibited there.

Following the illustration above, under the quasi-equilibrium approximation and the WTG approximation, the strength of the convection over the substellar region is constrained by the MSE difference between the near-surface and the free troposphere, and the fraction of the convective (as well as non-convective) area could be mainly determined by the zonal MSE gradient.

In the first group, the increased strengths of the convection and the large-scale mean circulation could be explained by the enhanced MSE difference between the near surface and the free troposphere over the substellar region (Figure 9(a)). The narrowing trend of the convection area could be explained by the relatively larger increase of MSE over the substellar region than that on the nightside (Figure 8(a)). This is because when the surface temperature rises by the same magnitude, water vapor acts as an amplifier (Figure 9(c)) since the saturated water vapor mixing ratio follows a strongly non-linear Clausius–Clapeyron relation with air temperature. The enhanced day-night MSE contrast results in a larger MSE inversion outside the convecting substellar area (see dashed lines in Figure 9(a)), thus suppressing the convection more effectively and leading to the narrowing trend of the ascending area.

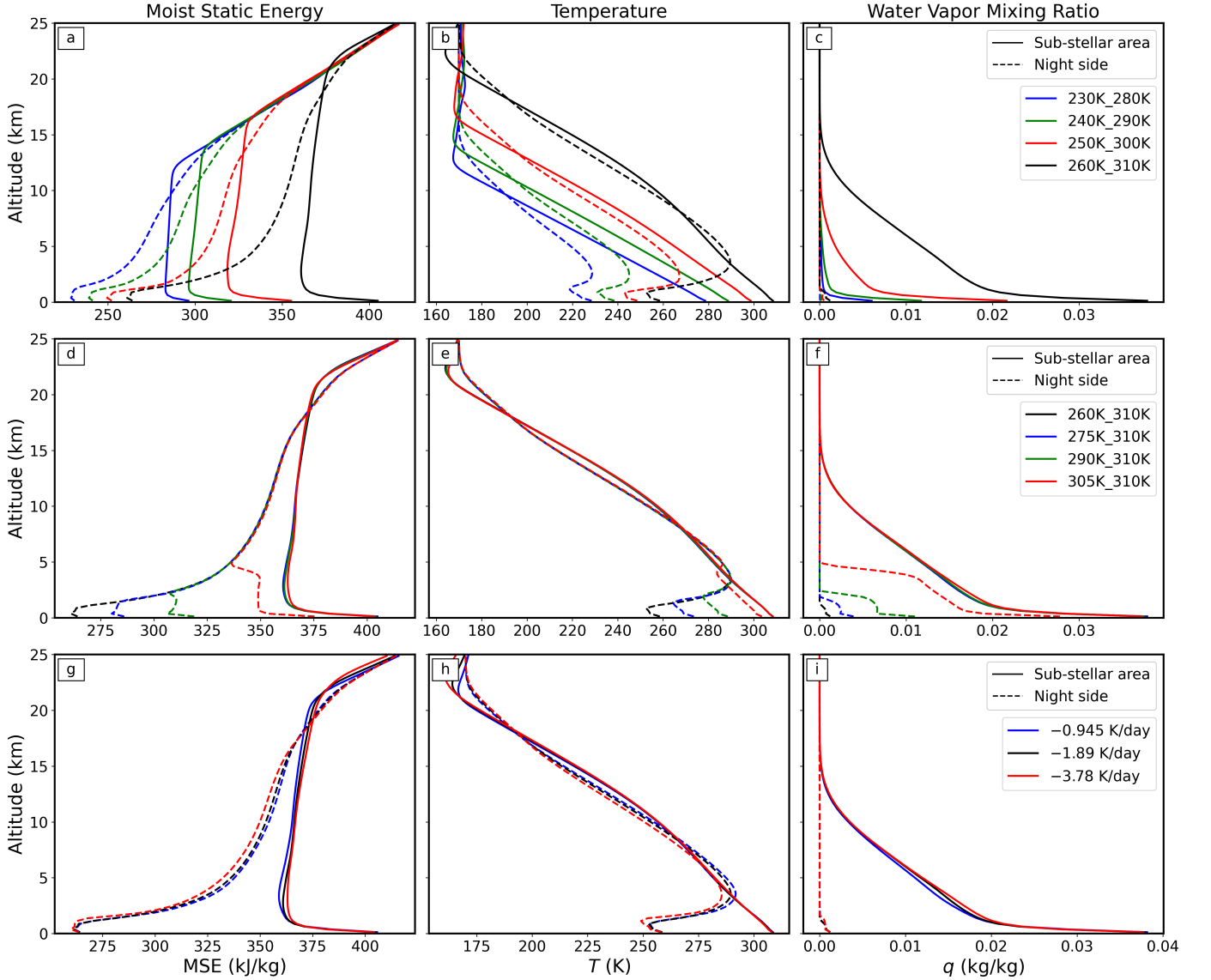


Figure 9. Vertical profiles of the three groups of experiments. The left column is MSE profiles, the center column is air temperature profiles, and the right column is water vapor mixing ratio. Solid lines are for the area mean over the substellar region (representing the ascending branch of the large-scale atmospheric overturning circulation), and dashed lines are for the area mean over the nightside (representing the descending branch). (a-c) uniformly changing the surface temperature, (d-f) changing the day-night surface temperature contrast, and (g-i) changing the radiative cooling rate.

In the second group, the widening trends of the convective cloud area and of the ascending branch of the large-scale circulation are due to the decrease of the MSE contrast between the substellar area and the rest region (Figures 8(b) & 9(d)). (1): MSE at the near surface of the nightside increases a lot, due to the direct effect of the warming on the nightside (Figure 9(e)); the increase of water vapor on the nightside also acts to amplify the night-side near-surface MSE and reduce the day-night MSE contrast (Figure 9(f)). (2): In the free troposphere, the thermodynamic profiles including MSE, temperature, and water vapor remain nearly the same for both dayside and nightside, when reducing the day-night contrast (Figure 9(d-f)). This is because surface temperature over the

substellar area nearly does not change, and because of the strong constraints of the quasi-equilibrium approximation and the WTG approximation. This means that the substellar surface temperature determines not only thermal properties near the surface but also those in the entire free troposphere. Strong convection links the free troposphere to the surface and the WTG approximation links the substellar area to the rest region in the free troposphere. (3): Due to the combination of (1) and (2), the vertical MSE inversion on the nightside decreases. Therefore, the suppression of convection is weakened, and the convection area expands towards the nightside. Moreover, the weakening of the atmospheric circulation can also be understood using the constrain of energy transport. Due to the constrain of the WTG approximation and the reduced day-night MSE contrast, less energy is required to be transported from the substellar region to the nightside. As the ascending branch becomes wider, the weakening of its strength is necessary.

In the third group, the widening trends of the convective clouds and the ascending branch of the large-scale circulation are constrained by horizontal energy transport. On the dayside, the main energy balance of the atmosphere is between latent heat release, radiative cooling, and horizontal energy output to the nightside (Yang & Abbot 2014). On the nightside, the main energy balance is between radiative cooling and horizontal energy input from the dayside. For global mean, the dominated balance is between latent heat release and radiative cooling (note that there is no explicit shortwave or longwave radiation in all the experiments of this study). When the radiative cooling is increased, on one hand, the magnitude of the latent heat release needs to increase in order to balance the increased radiative cooling. This implies increases in the strengths of convection and large-scale circulation, as found in Figure 6(e-g and i-k). On the other hand, the profiles of MSE, air temperature, and water vapor nearly do not change (Figure 9(g-i)). This implies that the atmospheric heat transport is so effective in maintaining the weak temperature gradients. So, the strength of the large-scale circulation needs to increase to balance the enhanced radiative cooling on the nightside. Moreover, the enhanced radiative cooling directly drives stronger downwelling on the nightside and increases the global overturning circulation; in the following section, we will more exactly show how the radiative cooling directly influences the strength of the downwelling branch.

Furthermore, the latent heat release increases but with a smaller magnitude than that of the increase of radiative cooling rate. This can be found in Figure 4(f): when the radiative cooling rate is doubled, the magnitude of the rainfall rate (equaling to the latent heat release over the constant of specific latent heat (L_v)) increases by only about 30%. This is likely limited by the unchanged surface temperature in this group of experiments. The relatively smaller magnitude increase in latent heat release implies that the widths of the convective area and the ascending branch of the large-scale circulation are required to increase.

3.3. *What Determines the Width of the High-level Anvil Clouds?*

In subsection 3.1, we have shown that the width of the high-level anvil clouds shrinks as the surface temperature uniformly increases, but expands when reducing the day-night temperature contrast or increasing the radiative cooling rate. Below, we show that this can be qualitatively explained using radiation-driven divergence, generally following the idea of Bony et al. (2016) and Cronin & Wing (2017). The high-level anvil clouds in the upper troposphere of the dayside are transported from the substellar convective area towards the nightside. This outflow is closely related to mass divergence. Based on mass conservation, horizontal divergence (D_r) is equal to $\frac{\partial \omega_r}{\partial p}$, where ω_r is the

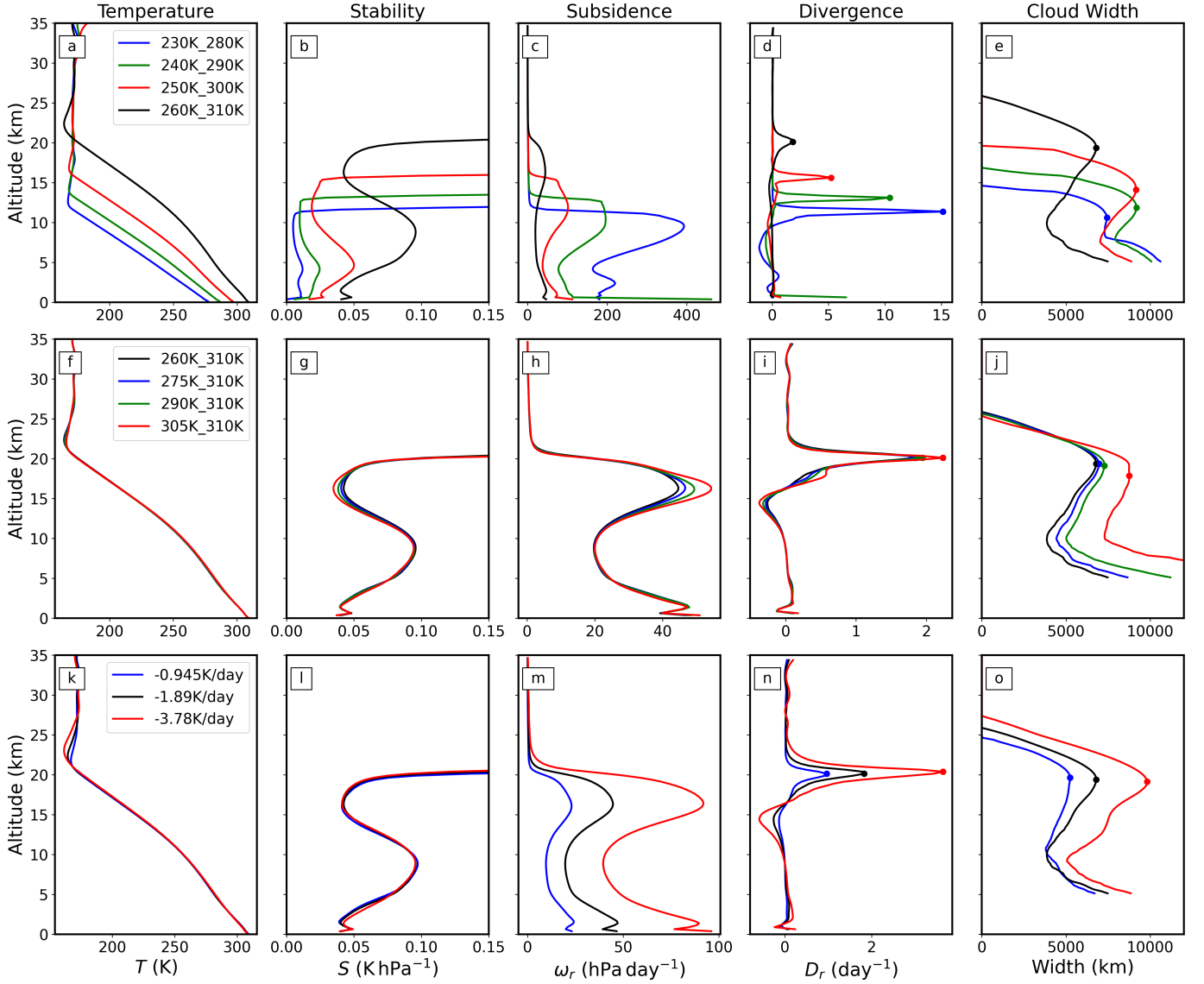


Figure 10. The mechanism that determines the width of the high-level anvil clouds. The first column is the vertical temperature profiles over the substellar area, the second column is the atmospheric stability, the third column is the radiation-driven vertical velocity (Equation (12)), the fourth column is the corresponding horizontal divergence, and the fifth column is the cloud width simulated by the model SNAP. The cloud width is defined as the width of the area with temporally-averaged cloud water mixing ratio larger than $10^{-6} \text{ kg kg}^{-1}$. The dots in the fourth and fifth columns mark the peak of the curves. The upper row is for the experiments of uniformly changing the surface temperature, the middle row is for the experiments of changing the day-night temperature contrast, and the lower row is for the experiments of changing the radiative cooling rate.

vertical velocity in pressure coordinate, and p is air pressure (Vallis 2017). The value of ω_r could be obtained from the temperature equation in an equilibrium state. Under the WTG approximation, the horizontal temperature gradients can be ignored, so the vertical velocity (ω_r) is approximately equal to:

$$\omega_r \cong -\frac{Q_r}{S}, \quad (12)$$

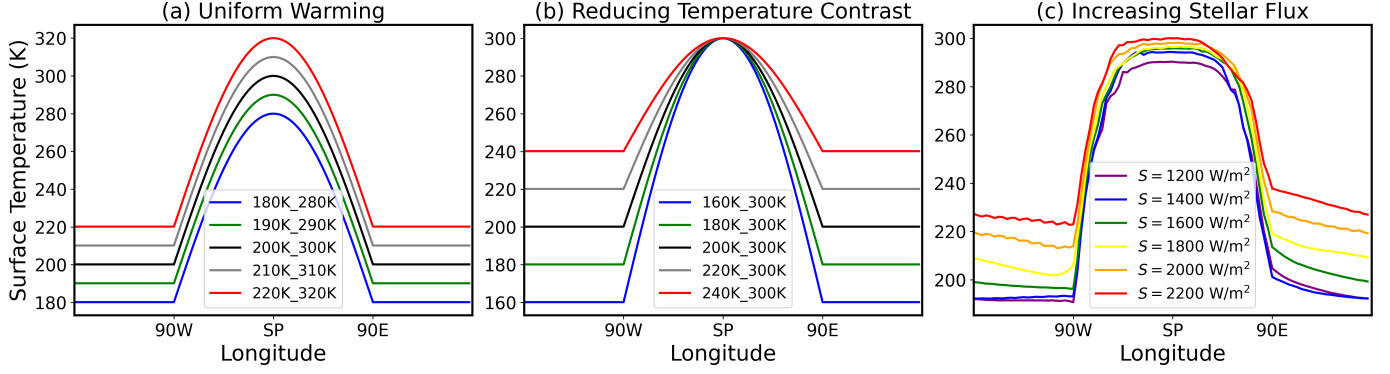


Figure 11. Surface temperature distribution in the GCM experiments. Panel (a) shows the specified surface temperatures in the group of uniformly warming or cooling the surface by intervals of 10 K; panel (b) shows the specified surface temperatures in the group of reducing the day-night contrast; and panel (c) shows the obtained surface temperatures in the simulations coupled to a 50-m slab ocean. These plots show the meridional-mean surface temperatures from 90°S and 90°N . Note that in panel (b) the meridional-mean surface temperatures in the substellar region also increase significantly, due to that this figure is for the mean from 90°S to 90°N , and both the day-night surface temperature contrast and the equator-pole surface temperature contrast decrease in this group of experiments.

where Q_r is the radiative cooling rate, and S is the atmospheric stability (Emanuel et al. 1994; Bony et al. 2016). The value of S is defined as $-\frac{T}{\theta} \frac{\partial \theta}{\partial p}$, where T is air temperature, and θ is potential temperature. Therefore, the width of the outflow (assuming to be proportional to the width of the high-level anvil clouds) is mainly determined by two factors: the strength of the radiative cooling and the atmospheric stability (Bony et al. 2016). The vertical profiles of T , S , ω_r , D_r , and the width of the high-level anvil clouds are shown in Figure 10.

In the first group of experiments, the width of the high-level anvil clouds generally decreases with uniformly increasing the surface temperature (Figure 10(e)). This is mainly due to the increase of atmospheric stability (S , Figure 10(b)), and thereby the radiation-driven divergence becomes weaker (Figure 10(d)). The increase of S is due to the fact that the warming of the atmosphere is larger than the warming of the surface, just following the moist adiabatic process. Note that the altitude of the anvil clouds exhibits a significant upward shift with surface warming. This is because the atmospheric convection reaches higher altitudes. In the second group, the width of the high-level anvil clouds increases when the day-night surface temperature contrast decreases (Figure 10(j)). It is due to the decrease of the atmospheric stability in the altitudes around 15–20 km (Figure 10(g)). In the third group, the width of the high-level anvil clouds increases with enhancing radiative cooling rate in the atmosphere (Figure 10(o)). This is due to the direct effect of increasing the value of Q_r in Equation (12), although the air temperature and the stability nearly do not change (Figure 10(k,l)). The latter is mainly determined by the surface temperature that is fixed in this group of experiments.

3.4. Results of the 3D GCM Simulations

In order to compare the results of CRM simulations to the results of GCMs, we did three corresponding groups of experiments using a GCM, CAM3. In the first group, the surface temperatures are specified as shown in Figure 11(a), and five cases are considered with uniformly varying the surface temperatures by 10 K in each case. This group is corresponding to the first group of CRM. In the

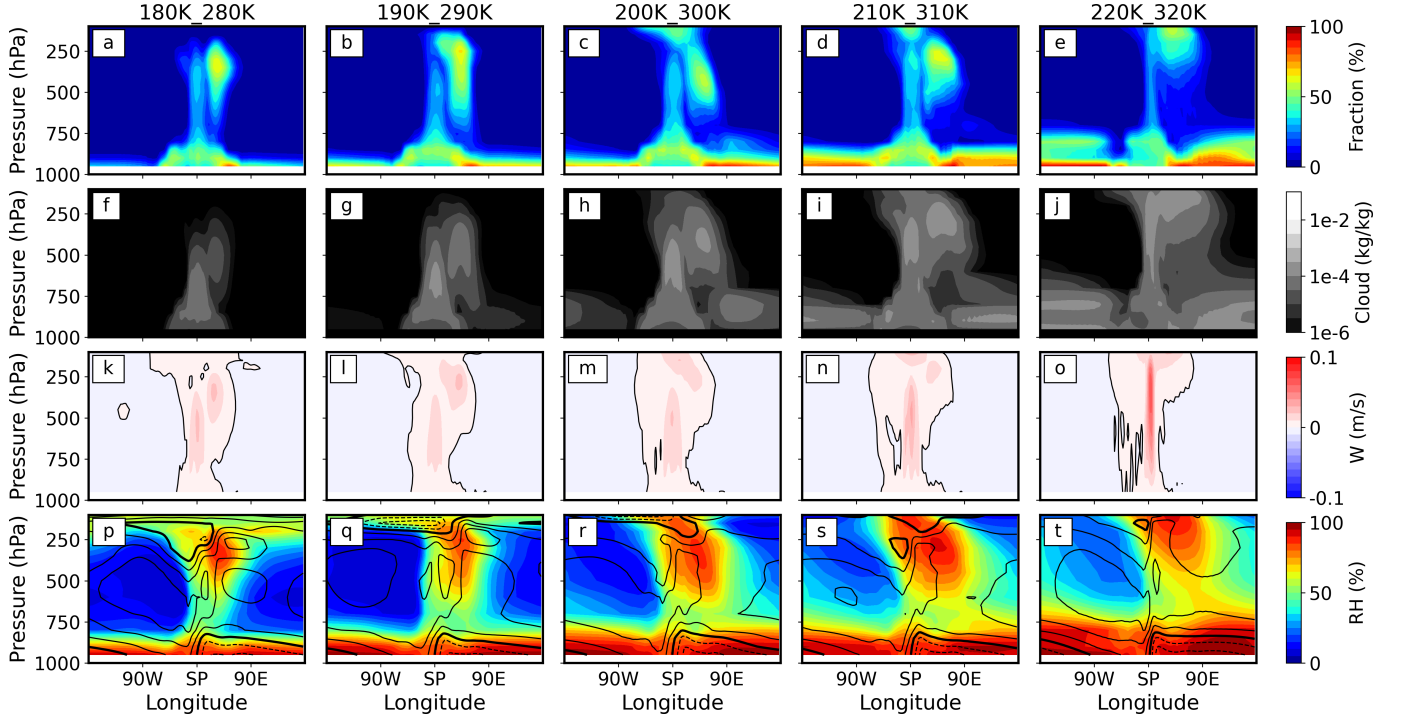


Figure 12. Meridional-mean values from 90°S and 90°N for (a-e) cloud fraction, (f-j) cloud water concentration, (k-o) vertical velocity, and (p-t) relative humidity (color shaded) and zonal wind (contour lines with intervals of 5 m s^{-1} , bold zero-value line, and dashed negative lines) in the GCM experiments of uniformly changing the surface temperatures. Each column represents an experiment, and the minimum and maximum surface temperatures are denoted on the top of each column. For the specified surface temperatures, please see Figure 11(a).

second group, the surface temperature at the substellar point is fixed (300 K), while the night-side surface temperatures are changed by 20 K in each case, as shown in Figure 11(b). This group is corresponding to the second group in the CRM experiments, although not 100% similarity. In the third group, the surface is coupled to a 50-m slab ocean, rather than with fixed surface temperatures. Six experiments are performed, in which the stellar flux is increased by 200 W m^{-2} in each case. The results of the surface temperatures are shown in Figure 11(c). It is clear to see that the surface temperatures of both dayside and nightside increase with increasing stellar flux, and the night-side warming is stronger than the day-side warming. The results of these three groups of experiments are shown in Figures 12, 13, and 14, respectively. Because realistic radiation transfer is included in the GCM, no experiment of fixed radiative cooling was performed.

In the first group of the GCM experiments, the cloud fraction, cloud water concentration, and vertical velocity become generally larger when the surface is uniformly warmed (Figure 12(a-o)). But, the width of the ascending branch of the large-scale circulation decreases, as clearly seen in Figure 12(k-o). These trends are roughly consistent with those found in the first group of CRM experiments (Figure 3(f-h and j-l)).

In the second group of the GCM experiments, when the day-night surface temperature contrast is reduced, the convective cloud area becomes wider (Figure 13(a-j)), but the strength of the ascending branch of the large-scale circulation becomes smaller (Figure 13(k-o)). Surprisingly, these trends

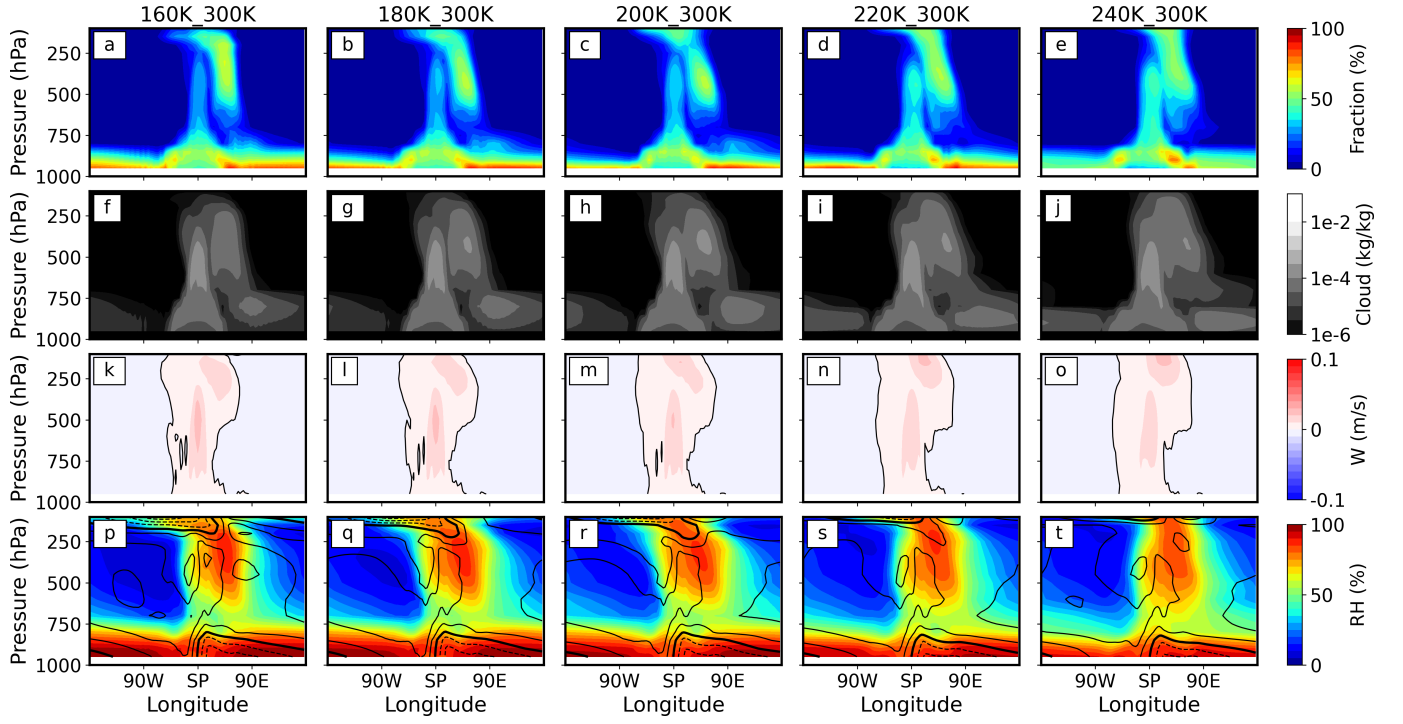


Figure 13. Same as Figure 12 but for the GCM experiments of changing the day-night surface temperature contrast. For the specified surface temperatures, please see Figure 11(b).

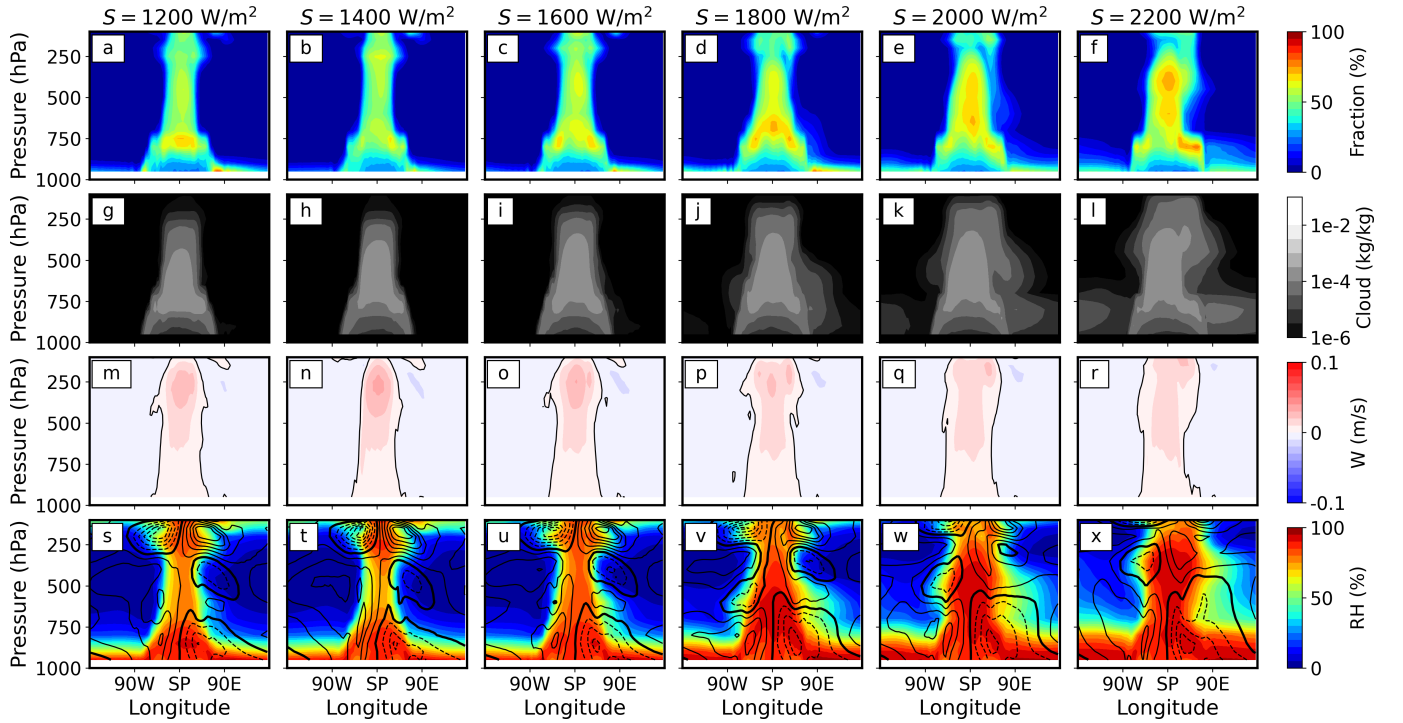


Figure 14. Same as Figure 12 but for the GCM experiments coupled to a 50-m slab ocean with varying stellar flux. For the obtained surface temperatures, please see Figure 11(c).

are also qualitatively consistent with those found in the second group of the CRM experiments (Figure 5(e-l)).

In the third group of the GCM experiments, when the stellar flux is increased, the width of the ascending branch of the large-scale circulation increases (Figure 14(m-r)). The strength of the large-scale circulation does not show a clear trend. Cloud fraction (Figure 14(a-f)), cloud water concentration (Figure 14(g-l)), and relative humidity (Figure 14(s-x)) increase significantly with increasing the stellar flux.

Although the global view and the general trends are broadly similar between these two types of models, there are still several significant differences. (1) There are more eddies and random structures in the 3D GCM experiments due to the existence of waves, baroclinic eddies, and the effect of the Coriolis force, whereas all of these are not included in the 2D CRM simulations. (2) The mean zonal winds in the free troposphere of the 3D GCM are in the direction from west to east, or called equatorial superrotation (see the contour lines in the bottom panels of Figures 12, 13, and 14). The superrotation is maintained by eddy momentum transport from extra-tropics to tropics, ultimately driven by the uneven stellar flux distribution between the dayside and the nightside (Showman & Polvani 2010, 2011; Pierrehumbert & Hammond 2019). The eddy momentum transport and equatorial superrotation are absent in the 2D simulations. (3) The asymmetry between the west side and the east side of the substellar point is large in the 3D GCM experiments, such as that there are more clouds on the east side than on the west side, and the high relative humidity region also tilts towards the east side. This is mainly due to the combined effects of waves, instabilities, and the equatorial superrotation. But, in the 2D CRM experiments, the symmetry between the west side and the east side is almost perfect. (4) In the 2D CRM, the trend of the convective cloud area is well consistent with the trend in the area of the upwelling branch of the large-scale circulation, but in the GCM, the influence of the equatorial superrotation on the extension of the high-level clouds is so strong that the trends of these two fields are not always synchronous. (5) Due to the simple boundary layer scheme used in the CRM simulations, the depth of the near-surface branch of the large-scale circulation is much larger than that in the GCM, $\approx 6\text{--}10$ km versus $\approx 2\text{--}5$ km. Based on previous studies, a shallow boundary layer is more reliable (Wordsworth 2015; Koll & Abbot 2016).

4. SUMMARY

The simplified 2D cloud-resolving model, SNAP, was employed to investigate the general characters of clouds and atmospheric circulation and the effects of varying surface temperature and infrared radiation on the convection and clouds of tidally locked habitable planets. The main results are summarized as follows:

1. Stimulated by the centrally-peaked surface temperature pattern and the uniform radiative cooling, we obtain a global-scale Walker-like circulation and optically thick clouds in the substellar area on the dayside of the planet.
2. When uniformly increasing the surface temperature, the ascending area narrows mainly due to the increased MSE contrast between the substellar area and the nightside. The width of high-level anvil clouds also decreases, mainly due to the increase of atmospheric stability. But, the strengths of convection and large-scale circulation increase, due to the increased MSE difference between the near surface and the free troposphere.

3. When the day-night surface temperature contrast is decreased, the convection and large-scale circulation become weaker in strength but wider in area. These could be explained by the decrease of the day-night MSE contrast.
4. When the radiative cooling rate is increased, convection and large-scale circulation become stronger, and the convection area and the width of high-level anvil clouds increase. These can be explained based on the global energy budget and radiation-driven downwelling and divergence.
5. The results of 2D cloud-resolving experiments are broadly similar to those in corresponding 3D GCM experiments, although there are many significant differences. This bolsters the use of GCMs in exoplanetary climate and habitability studies.

The weaknesses of the cloud-resolving simulations shown here are: the simulation domain is 2D along the equator rather than a real 3D sphere, and the effect of the Coriolis force is not included, the radiative transfer module is so simple that realistic radiative transfer is absent, the cloud microphysical processes are very simple, and the surface temperature is fixed rather than coupled to the atmosphere or the ocean. Future 3D simulations including realistic radiative transfer and a coupled slab ocean or dynamical ocean will be better to represent the climate system of a tidally locked habitable planet.

The results of the three groups of CRM experiments suggest that cloud water amount and cloud coverage would likely increase when the stellar flux is increased if realistic radiative transfer were included in the model. This can cause a stabilizing cloud feedback and make the inner edge of the habitable zone closer to the host star, as suggested by previous GCM simulations (e.g. [Yang et al. 2013](#); [Kopparapu et al. 2016](#)). Further work is required to confirm this using a 3D CRM with realistic radiative transfer and more complex cloud microphysical schemes.

ACKNOWLEDGMENTS

We are grateful to Bolei Yang and Zhihong Tan for their helpful suggestions. We also thank Xinyi Song for helping with the language revision. J.Y. acknowledges support from the National Natural Science Foundation of China (NSFC) under grants 42075046, 41888101, and 41675071.

APPENDIX

Here we perform three extra groups of sensitivity tests in order to test the effects of boundary layer friction and two microphysical parameters. These results below suggest that boundary layer scheme and microphysical parameters can strongly influence the simulated results of clouds, although these parameters do not completely change the basic feature of the large-scale circulation and convection.

The effect of the boundary layer friction is tested in three experiments in which we set the time scale of friction-induced momentum damping as 2 hrs, 12 hrs, and infinite long (i.e., free-slip surface), respectively. A longer time scale means a weaker friction effect. The results of cloud water concentration are shown in Figure 15(a-c). As the friction weakens, the convective area and the

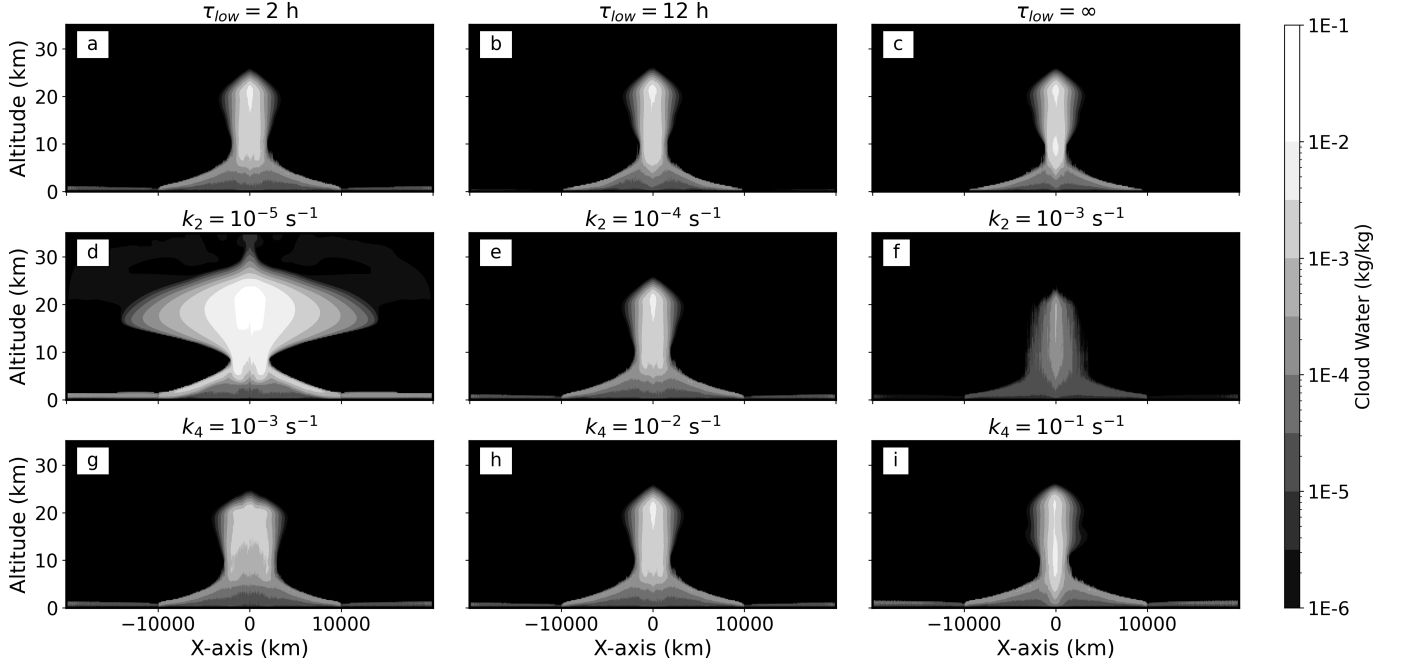


Figure 15. Cloud water concentration in the sensitivity tests of (a-c) varying the surface friction time scale (τ_{low} in Equation (10)), (d-f) varying the conversion rate from cloud water to precipitating water (k_2), and (g-i) varying the re-evaporation rate of rain droplets back to water vapor (k_4). Each panel represents an experiment, and its corresponding parameter is marked at the top of the panel.

ascending branch of the large-scale circulation become narrower, similar to that found in Liu & Moncrieff (2008). Weaker surface friction leads to stronger near-surface horizontal winds and more centralized convergences, so the ascending branch becomes narrower. In the default experiment, the inflow winds have maximum strength at the level of about 1 km. In the free-slip experiment, the maximum winds reach the lowest level of the model, and the temperature inversion penetrates to the surface, leaving no space for night-side cloud formation; as shown in Figure 15(c), there are no night-side clouds in this experiment.

The microphysical processes in the model are described in Equations (7)–(9), in which k_2 means the cloud-to-precipitation conversion rate. A larger k_2 means a quicker conversion from cloud water to precipitating water. We change k_2 within two orders of magnitude, and the resulting cloud water concentration is shown in Figure 15(d-f). As k_2 increases, cloud water concentration decreases strongly, and the width of the high-level anvil clouds becomes narrower significantly, due to the direct effect of a faster transition from clouds to rainfall. However, the domain-average rainfall remains nearly the same in these experiments (figure not shown) because the latent heat release must balance the radiative cooling, which is fixed.

The re-evaporation rate of precipitating water (k_4) also affects the results. A larger k_4 means a quicker re-evaporation from rain droplets to water vapor under an unsaturated environment. We change k_4 within two orders of magnitude, and the resulting cloud water concentration is shown in Figure 15(g-i). As k_4 increases, the convective area and the ascending branch of the large-scale circulation become narrower. The reason is that enhanced re-evaporation and related heat absorption

reduce the magnitude of diabatic heating, suppressing convective activities, narrowing the ascending area, and reducing the convective cloud area.

REFERENCES

- Arakawa, A., & Schubert, W. H. 1974, *Journal of the Atmospheric Sciences*, 31, 674, doi: [10.1175/1520-0469\(1974\)031<0674:IOACCE>2.0.CO;2](https://doi.org/10.1175/1520-0469(1974)031<0674:IOACCE>2.0.CO;2)
- Bony, S., Stevens, B., Coppin, D., et al. 2016, *Proceedings of the National Academy of Sciences*, 113, 8927, doi: [10.1073/pnas.1601472113](https://doi.org/10.1073/pnas.1601472113)
- Boutle, I. A., Mayne, N. J., Drummond, B., et al. 2017, *Astronomy & Astrophysics*, 601, A120, doi: [10.1051/0004-6361/201630020](https://doi.org/10.1051/0004-6361/201630020)
- Bretherton, C. S., Blossey, P. N., & Peters, M. E. 2006, *Theoretical and Computational Fluid Dynamics*, 20, 421, doi: [10.1007/s00162-006-0029-7](https://doi.org/10.1007/s00162-006-0029-7)
- Bretherton, C. S., & Khairoutdinov, M. F. 2015, *Journal of Advances in Modeling Earth Systems*, 7, 1765, doi: [10.1002/2015MS000499](https://doi.org/10.1002/2015MS000499)
- Bretherton, C. S., & Sobel, A. H. 2002, *Journal of Climate*, 15, 2907, doi: [10.1175/1520-0442\(2002\)015<2907:ASMOAC>2.0.CO;2](https://doi.org/10.1175/1520-0442(2002)015<2907:ASMOAC>2.0.CO;2)
- Briegleb, B. P. 1992, *Journal of Geophysical Research: Atmospheres*, 97, 7603, doi: [10.1029/92JD00291](https://doi.org/10.1029/92JD00291)
- Byrne, M. P., & Schneider, T. 2016, *Journal of Climate*, 29, 4709, doi: [10.1175/JCLI-D-15-0767.1](https://doi.org/10.1175/JCLI-D-15-0767.1)
- Charney, J. G. 1963, *Journal of the Atmospheric Sciences*, 20, 607, doi: [10.1175/1520-0469\(1963\)020<0607:ANOLSM>2.0.CO;2](https://doi.org/10.1175/1520-0469(1963)020<0607:ANOLSM>2.0.CO;2)
- Chen, Y.-T., & Wu, C.-M. 2019, *Journal of Advances in Modeling Earth Systems*, 11, 3321, doi: [10.1029/2019MS001762](https://doi.org/10.1029/2019MS001762)
- Collins, W. D., Rasch, P. J., Boville, B. A., et al. 2004, NCAR Technical Note, TN-464+STR
- Cronin, T. W., & Wing, A. A. 2017, *Journal of Advances in Modeling Earth Systems*, 9, 2883, doi: [10.1002/2017MS001111](https://doi.org/10.1002/2017MS001111)
- Del Genio, A. D., Way, M. J., Amundsen, D. S., et al. 2019, *Astrobiology*, 19, 99, doi: [10.1089/ast.2017.1760](https://doi.org/10.1089/ast.2017.1760)
- Edson, A., Lee, S., Bannon, P., Kasting, J. F., & Pollard, D. 2011, *Icarus*, 212, 1, doi: [10.1016/j.icarus.2010.11.023](https://doi.org/10.1016/j.icarus.2010.11.023)
- Emanuel, K. 2007, *The Global Circulation of the Atmosphere*, 186
- Emanuel, K. A., David Neelin, J., & Bretherton, C. S. 1994, *Quarterly Journal of the Royal Meteorological Society*, 120, 1111, doi: [10.1002/qj.49712051902](https://doi.org/10.1002/qj.49712051902)
- Fauchez, T. J., Turbet, M., Wolf, E. T., et al. 2020, *Geoscientific Model Development*, 13, 707, doi: [10.5194/gmd-13-707-2020](https://doi.org/10.5194/gmd-13-707-2020)
- Grabowski, W. W., Yano, J.-I., & Moncrieff, M. W. 2000, *Journal of the Atmospheric Sciences*, 57, 2022, doi: [10.1175/1520-0469\(2000\)057<2022:CRMOTC>2.0.CO;2](https://doi.org/10.1175/1520-0469(2000)057<2022:CRMOTC>2.0.CO;2)
- Hack, J. J., Boville, B. A., Briegleb, B. P., et al. 1993, *Description of the NCAR community climate model (CCM2)*, Tech. Rep. NCAR/TN-382+STR, University Corporation for Atmospheric Research, doi: [10.5065/D6QZ27XV](https://doi.org/10.5065/D6QZ27XV)
- Haqq-Misra, J., Wolf, E. T., Joshi, M., Zhang, X., & Kopparapu, R. K. 2018, *The Astrophysical Journal*, 852, 67, doi: [10.3847/1538-4357/aa9f1f](https://doi.org/10.3847/1538-4357/aa9f1f)
- Joshi, M., Haberle, R., & Reynolds, R. 1997, *Icarus*, 129, 450, doi: [10.1006/icar.1997.5793](https://doi.org/10.1006/icar.1997.5793)
- Kessler, E. 1969, in *On the distribution and continuity of water substance in atmospheric circulations* (Springer), 1–84, doi: [10.1007/978-1-935704-36-2_1](https://doi.org/10.1007/978-1-935704-36-2_1)
- Khairoutdinov, M. F., & Emanuel, K. 2018, *Journal of the Atmospheric Sciences*, 75, 4337, doi: [10.1175/JAS-D-18-0152.1](https://doi.org/10.1175/JAS-D-18-0152.1)
- Kiehl, J., Hack, J., Bonan, G., et al. 1998, *Journal of Climate*, 11, 1131, doi: [10.1175/1520-0442\(1998\)011<1131:TNCFAR>2.0.CO;2](https://doi.org/10.1175/1520-0442(1998)011<1131:TNCFAR>2.0.CO;2)
- Klemp, J. B., & Wilhelmson, R. B. 1978, *Journal of the Atmospheric Sciences*, 35, 1070, doi: [10.1175/1520-0469\(1978\)035<1070:TSOTDC>2.0.CO;2](https://doi.org/10.1175/1520-0469(1978)035<1070:TSOTDC>2.0.CO;2)

- Koll, D. D. B., & Abbot, D. S. 2016, *The Astrophysical Journal*, 825, 99, doi: [10.3847/0004-637x/825/2/99](https://doi.org/10.3847/0004-637x/825/2/99)
- Kopparapu, R. k., Wolf, E. T., Arney, G., et al. 2017, *The Astrophysical Journal*, 845, 5, doi: [10.3847/1538-4357/aa7cf9](https://doi.org/10.3847/1538-4357/aa7cf9)
- Kopparapu, R. k., Wolf, E. T., Haqq-Misra, J., et al. 2016, *The Astrophysical Journal*, 819, 84, doi: [10.3847/0004-637x/819/1/84](https://doi.org/10.3847/0004-637x/819/1/84)
- Lefèvre, M., Turbet, M., & Pierrehumbert, R. 2021, 3D convection-resolving model of temperate, tidally-locked exoplanets. <https://arxiv.org/abs/2104.05559>
- Li, C., & Chen, X. 2019, *The Astrophysical Journal Supplement Series*, 240, 37, doi: [10.3847/1538-4365/aafdaa](https://doi.org/10.3847/1538-4365/aafdaa)
- Liu, C., & Moncrieff, M. 2008, *J. Geophys. Res.*, 113, doi: [10.1029/2008JD010206](https://doi.org/10.1029/2008JD010206)
- Marquet, P. 1993, *Quarterly Journal of the Royal Meteorological Society*, 119, 567, doi: [10.1002/qj.49711951112](https://doi.org/10.1002/qj.49711951112)
- Menou, K. 2013, *The Astrophysical Journal*, 774, 51, doi: [10.1088/0004-637X/774/1/51](https://doi.org/10.1088/0004-637X/774/1/51)
- Merlis, T. M., & Schneider, T. 2010, *Journal of Advances in Modeling Earth Systems*, 2, doi: [10.3894/JAMES.2010.2.13](https://doi.org/10.3894/JAMES.2010.2.13)
- Miller, M., & Pearce, R. 1974, *Quarterly Journal of the royal meteorological society*, 100, 133, doi: [10.1002/qj.49710042402](https://doi.org/10.1002/qj.49710042402)
- Muller, C. J., & Held, I. M. 2012, *Journal of the Atmospheric Sciences*, 69, 2551, doi: [10.1175/JAS-D-11-0257.1](https://doi.org/10.1175/JAS-D-11-0257.1)
- Narenpitak, P., & Bretherton, C. S. 2019, *Journal of Advances in Modeling Earth Systems*, 11, 1600, doi: [10.1029/2018MS001572](https://doi.org/10.1029/2018MS001572)
- Neelin, J. D., Peters, O., Lin, J. W.-B., Hales, K., & Holloway, C. E. 2008, *Philosophical Transactions of the Royal Society A: Mathematical, Physical and Engineering Sciences*, 366, 2579, doi: [10.1098/rsta.2008.0056](https://doi.org/10.1098/rsta.2008.0056)
- Pierrehumbert, R. T. 2010, *Principles of planetary climate* (Cambridge University Press), doi: [10.1017/CBO9780511780783](https://doi.org/10.1017/CBO9780511780783)
- Pierrehumbert, R. T., & Hammond, M. 2019, *Annual Review of Fluid Mechanics*, 51, 275, doi: [10.1146/annurev-fluid-010518-040516](https://doi.org/10.1146/annurev-fluid-010518-040516)
- Ramanathan, V., & Downey, P. 1986, *Journal of Geophysical Research: Atmospheres*, 91, 8649, doi: [10.1029/JD091iD08p08649](https://doi.org/10.1029/JD091iD08p08649)
- Rasch, P. J., & Kristjánsson, J. E. 1998, *Journal of Climate*, 11, 1587, doi: [10.1175/1520-0442\(1998\)011<1587:ACOTCM>2.0.CO;2](https://doi.org/10.1175/1520-0442(1998)011<1587:ACOTCM>2.0.CO;2)
- Salameh, J. 2017, PhD thesis, Universität Hamburg, Hamburg, doi: [10.17617/2.2482990](https://doi.org/10.17617/2.2482990)
- Sergeev, D. E., Lambert, F. H., Mayne, N. J., et al. 2020, *The Astrophysical Journal*, 894, 84, doi: [10.3847/1538-4357/ab8882](https://doi.org/10.3847/1538-4357/ab8882)
- Showman, A. P., & Polvani, L. M. 2010, *Geophysical Research Letters*, 37, doi: [10.1029/2010GL044343](https://doi.org/10.1029/2010GL044343)
- . 2011, *The Astrophysical Journal*, 738, 71, doi: [10.1088/0004-637x/738/1/71](https://doi.org/10.1088/0004-637x/738/1/71)
- Slingo, J. M. 1987, *Quarterly Journal of the Royal Meteorological Society*, 113, 899, doi: [10.1002/qj.49711347710](https://doi.org/10.1002/qj.49711347710)
- Sobel, A. H., Nilsson, J., & Polvani, L. M. 2001, *Journal of the atmospheric sciences*, 58, 3650, doi: [10.1175/1520-0469\(2001\)058<3650:TWTGAA>2.0.CO;2](https://doi.org/10.1175/1520-0469(2001)058<3650:TWTGAA>2.0.CO;2)
- Stevens, B., Satoh, M., Auger, L., et al. 2019, *Progress in Earth and Planetary Science*, 6, 1, doi: [10.1186/s40645-019-0304-z](https://doi.org/10.1186/s40645-019-0304-z)
- Su, H., Jiang, J. H., Vane, D. G., & Stephens, G. L. 2008, *Geophysical Research Letters*, 35, doi: [10.1029/2008GL035888](https://doi.org/10.1029/2008GL035888)
- Sundqvist, H. 1988, in *Physically-based modelling and simulation of climate and climatic change* (Springer), 433–461, doi: [10.1007/978-94-009-3041-4_10](https://doi.org/10.1007/978-94-009-3041-4_10)
- Tao, W.-K., & Soong, S.-T. 1986, *Journal of the atmospheric sciences*, 43, 2653, doi: [10.1175/1520-0469\(1986\)043<2653:ASOTRO>2.0.CO;2](https://doi.org/10.1175/1520-0469(1986)043<2653:ASOTRO>2.0.CO;2)
- Tomita, H., Miura, H., Iga, S.-i., Nasuno, T., & Satoh, M. 2005, *Geophysical Research Letters*, 32, doi: [10.1029/2005GL022459](https://doi.org/10.1029/2005GL022459)
- Vallis, G. K. 2017, *Atmospheric and Oceanic Fluid Dynamics: Fundamentals and Large-Scale Circulation*, 2nd edn. (Cambridge University Press), doi: [10.1017/9781107588417](https://doi.org/10.1017/9781107588417)
- Wallace, J. M., & Hobbs, P. V. 2006, in *Atmospheric Science: An Introductory Survey*, second edition edn. (San Diego: Academic Press), 63–111, doi: [10.1016/B978-0-12-732951-2.50008-9](https://doi.org/10.1016/B978-0-12-732951-2.50008-9)
- Wofsy, J., & Kuang, Z. 2012, *Journal of Climate*, 25, 8090, doi: [10.1175/JCLI-D-11-00692.1](https://doi.org/10.1175/JCLI-D-11-00692.1)

- Wolf, E. T. 2017, *The Astrophysical Journal*, 839, L1, doi: [10.3847/2041-8213/aa693a](https://doi.org/10.3847/2041-8213/aa693a)
- Wordsworth, R. 2015, *The Astrophysical Journal*, 806, 180
- Wordsworth, R. D., Forget, F., Selsis, F., et al. 2010, *Astronomy & Astrophysics*, 522, A22, doi: [10.1051/0004-6361/201015053](https://doi.org/10.1051/0004-6361/201015053)
- Yang, J., & Abbot, D. S. 2014, *The Astrophysical Journal*, 784, 155, doi: [10.1088/0004-637x/784/2/155](https://doi.org/10.1088/0004-637x/784/2/155)
- Yang, J., Abbot, D. S., Koll, D. D. B., Hu, Y., & Showman, A. P. 2019a, *The Astrophysical Journal*, 871, 29, doi: [10.3847/1538-4357/aaf1a8](https://doi.org/10.3847/1538-4357/aaf1a8)
- Yang, J., Cowan, N. B., & Abbot, D. S. 2013, *The Astrophysical Journal Letters*, 771, L45, doi: [10.1088/2041-8205/771/2/L45](https://doi.org/10.1088/2041-8205/771/2/L45)
- Yang, J., Leconte, J., Wolf, E. T., et al. 2019b, *The Astrophysical Journal*, 875, 46, doi: [10.3847/1538-4357/ab09f1](https://doi.org/10.3847/1538-4357/ab09f1)
- . 2016, *The Astrophysical Journal*, 826, 222, doi: [10.3847/0004-637X/826/2/222](https://doi.org/10.3847/0004-637X/826/2/222)
- Zhang, G. J., & McFarlane, N. A. 1995, *Atmosphere-Ocean*, 33, 407, doi: [10.1080/07055900.1995.9649539](https://doi.org/10.1080/07055900.1995.9649539)
- Zhang, M., Lin, W., Bretherton, C. S., Hack, J. J., & Rasch, P. J. 2003, *Journal of Geophysical Research: Atmospheres*, 108, ACL 10, doi: [10.1029/2002JD002523](https://doi.org/10.1029/2002JD002523)
- Zhang, X., Tian, F., Wang, Y., Dudhia, J., & Chen, M. 2017, *The Astrophysical Journal Letters*, 837, L27, doi: [10.3847/2041-8213/aa62fc](https://doi.org/10.3847/2041-8213/aa62fc)